JOURNAL OF GEOPHYSICAL RESEARCH, VOL. 115, A07324, doi:10.1029/2009JA015053, 2010

Sources of the traveling ionospheric disturbances observed by the ionospheric TIDDBIT sounder near Wallops Island on 30 October 2007

Sharon L. Vadas[1] and Geoff Crowley[2]

Received 3 November 2009; revised 25 January 2010; accepted 22 March 2010; published 30 July 2010.

[1] We model the gravity waves (GWs) excited by Tropical Storm (TS) Noel at 0432 UT on 30 October 2007. Using forward ray tracing, we calculate the body forces which result from the saturation and dissipation of these GWs. We then analyze the 59 traveling ionospheric disturbances (TIDs) observed by the TIDDBIT ionospheric sounder at 0400-1000 UT near Wallops Island. These TIDs were located at the bottomside of the F layer at z = 230–290 km, had periods of τ_r = 15 to 90 min, horizontal wavelengths of λ_H = 100 to 3000 km, and horizontal phase speeds of c_H = 140 to 650 m/s. 33 (~60%) of the TIDs were propagating northwest(NW) and north(N)ward, from the direction of TS Noel 1700–2000 km away. We show that these TIDs were likely GWs. 40% of these GWs had phase speeds larger than 280m/s. This precluded a tropospheric source and suggested mesospheric and thermospheric sources instead. Using reverse ray tracing, we compare the GW locations with the regions of convective overshoot, mesospheric body forces, and thermospheric body forces. We identify 27 of the northwest/northward propagating GWs as likely being secondary GWs excited by thermospheric body forces. Three may have originated from mesospheric body forces, although this is much less likely. None are identified as primary GWs excited directly by TS Noel. 11 of these GWs with c_H < 205 m/s likely reflected near the tropopause prior to detection. This secondary GW spectrum peaks at λ_H ~ 100–300 km and c_H ~ 100–300 m/s. To our knowledge, this is the first identification and quantification of secondary GWs from thermospheric body forces.

Citation: Vadas, S. L., and G. Crowley (2010), Sources of the traveling ionospheric disturbances observed by the ionospheric TIDDBIT sounder near Wallops Island on 30 October 2007, *J. Geophys. Res.*, *115*, A07324, doi:10.1029/2009JA015053.

1. Introduction

[2] An instrumented sounding rocket was launched at 0412 UT (12:12 AM local time) on 30 October 2007 from Wallops Island, Virginia (75.47°W and 37.95°N) into a midlatitude spread-F (MSF) condition (P. Bhaneja et al., A comprehensive rocket and radar study of midlatitude spread F, submitted to *Journal of Geophysical Research*, 2010). This launch occurred approximately 7 hours after a period when the Kp index was high, with Kp = 5 at 18–21 UT on 29 October 2007. The launch was part of an experiment with the goal of understanding what triggers MSF, and was unique because no rocket had flown through MSF previously. The instruments on the rocket measured the neutral winds, electric field, and plasma density. The comprehensive ground-based instruments included a new Doppler radar system called TIDDBIT which utilizes three transmitters and one receiver to measure the propagation characteristics of traveling ionospheric disturbances (TIDs) in the bottomside F-region of the ionosphere (G. Crowley, F. Rodrigues, A. Reynolds, G. Earle, T. Bullett, and R. Bishop, TIDDBIT HF doppler sounder measurements of TIDs during the Wallops Island rocket launch of October 2007, in preparation, 2010). The TIDDBIT system collected data for about a month prior to the launch and for seven days afterward.

[3] During the 6 hour window from 0400-1000 UT on 30 October 2007, 59 TIDs with periods of 15 to 90 min were observed by TIDDBIT at a range of altitudes from z = 237 to 283 km. These waves spanned nearly all azimuths, except NEward. There are several reasons why these waves are of particular interest. First, 40% of these waves had $c_H \geq$ 280 m/s, and therefore could not have originated near the tropopause. Second, 60% of the waves were propagating NW/Nward from the direction of TS Noel; this included a large percentage of waves with $c_H \geq$ 280 m/s. Because these waves had $\tau_r \leq$ 90 min, this precluded a southern auroral source. Thus, a detailed examination of these waves and their sources are of particular interest because they may illuminate a thermospheric source of waves other than auroral heating.

[1] Colorado Research Associates Division, NorthWest Research Associates, Boulder, Colorado, USA.
[2] Atmospheric and Space Technology Research Associates, San Antonio, Texas, USA.

0148-0227/10/2009JA015053

[4] A recent modeling study [*Vadas and Liu*, 2009, hereafter VL09] showed that the dissipation of "primary" GWs from a deep convective plume creates a localized, short-duration thermospheric body force at $z \simeq 180$ km which (1) accelerates the neutral, horizontal wind by ~800–1200 m/s/hr for 20 min over a spatially localized region in the thermosphere, creating a "mean" wind perturbation of ~400 m/s that dissipates within ~4 hrs, and (2) excites large-scale, upward and downward-propagating secondary GWs and large-scale TIDs (LSTIDs) with $\lambda_H \simeq 2100$ km, $c_H \simeq 500$ m/s, and periods of $\tau_r \simeq 80$ min which propagate away from the body force as concentric, anti-symmetric rings to $z \gtrsim 420$ km. This result shared many similarities with the mean wind and secondary GWs excited by horizontal body forces in non-viscous fluids [*Zhu and Holton*, 1987; *Fritts and Luo*, 1992; *Luo and Fritts*, 1993; *Vadas and Fritts*, 2001; *Vadas et al.*, 2003, hereafter V03]. What is of particular interest here is that the secondary GWs propagated ~20° within an hour, and that the downward-propagating secondary GWs reflected upward at $z \sim 120$ km.

[5] Although VL09 could not resolve secondary GWs with $\lambda_H < 2000$ km, they argued that the secondary GW spectrum from this convective plume should peak at $\lambda_H \sim 800$–1300 km and $c_H \sim 200$–600 m/s, with significant amplitudes for waves with $\lambda_H \sim 200$ to 10000 km. However, that study did not consider the changes to the secondary GW spectrum when multiple convective plumes create smaller-scale variability of the thermospheric body forces because of constructive and destructive wave interference. Such forces are expected to excite secondary GWs with even smaller λ_H.

[6] The purpose of this paper is to model the GWs excited by convective overshoot in TS Noel, to calculate the resulting mesospheric and thermospheric body forces, to compare the properties of the TIDs observed by TIDDBIT with GW dissipative theory, and to determine the likely sources of the NW/Nward propagating TIDs. In section 2, we briefly describe our ray trace and convective plume models. We model the primary GWs excited by the overshooting convective plumes and clusters in section 3, and ray trace them into the mesosphere and thermosphere. We then calculate the mesospheric and thermospheric body forces which result. Section 4 describes the TIDDBIT instrument and observed TIDs, and compares the characteristics of the NW/Nward propagating TIDs with GW dissipative theory. In section 5, we reverse ray trace the TIDs in order to determine their most likely sources. In section 6, we show spectra of the identified secondary GWs. Our conclusions are contained in section 7.

2. Convective Plume and Ray Trace Models

2.1. Convective Plume Model

[7] Many non-linear models [*Piani et al.*, 2000; *Horinouchi et al.*, 2002; *Lane et al.*, 2001, 2003] and linear models [*Stull*, 1976; *Salby and Garcia*, 1987; *Alexander et al.*, 1995; *Walterscheid et al.*, 2001; *Beres*, 2004] of GW excitation from deep convection have been developed. Here, we use a linear model which describes the excitation of GWs from the envelope a convective plume which overshoots the tropopause and has a diameter $\mathcal{D}_H$ via an upward acceleration of air [*Vadas and Fritts*, 2004, 2009]. A convective cluster typically contains 2–4 plumes within a circle of diameter (3–4)$\mathcal{D}_{\rm H}$. Although the location of each plume within a cluster is highly individual, we define a cluster to be composed of 3 convective plumes in an equilateral triangle configuration, with a separation of $2.5\mathcal{D}_{\rm H}$ between the plume centers. The GWs excited by the plumes and clusters are high-frequency, and are described by the Boussinesq dispersion relation:

$$\omega_{Ir}^2 = \frac{k_H^2 N^2}{m^2 + k_H^2}, \tag{1}$$

where ω_{Ir} is the wave's intrinsic frequency, k, l, and m are the zonal, meridional, and vertical wave numbers, respectively, $k_H^2 = k^2 + l^2$, and N is the buoyancy frequency. The zonal, meridional, and vertical wavelengths are $\lambda_x = 2\pi/k$, $\lambda_y = 2\pi/l$, and $\lambda_z = 2\pi/m$, respectively. Additionally, the horizontal wavelength is $\lambda_H = 2\pi/k_H$. The GW's intrinsic frequency is related to its observed frequency, $\omega_r = 2\pi/\tau_r$, via

$$\omega_r = \omega_{Ir} + kU + lV = \omega_{Ir} + k_H U_H, \tag{2}$$

where U and V are the background zonal and meridional winds, respectively, and

$$U_H = (kU + lV)/k_H \tag{3}$$

is the background, neutral wind in the direction of GW propagation. The approximate amplitudes of the excited GWs with $\lambda_H \sim 20$–100 km and $\tau_r = 5$–15 min was verified by comparison with OH airglow observations [*Vadas et al.*, 2009a, 2009b]. We refer the reader to *Vadas and Fritts* [2009] for additional model details.

2.2. Ray Trace Model

[8] The GW dispersion relation we use for ray tracing is nonhydrostatic and compressible, but excludes acoustic waves. It includes the effects of kinematic viscosity and thermal diffusivity, the main sources of dissipation for high-frequency GWs with small amplitudes [*Vadas and Fritts*, 2005, hereafter VF05]. We do not allow ω_r to vary in time; this follows the assumption that the background temperatures and winds vary slowly in time. We note that some formulations include changing ω_r with time [e.g., *Jones*, 1969]. We refer the reader to VF05 and *Vadas* [2007, hereafter V07] for model details.

[9] The convective plume model outputs the amplitudes, scales, intrinsic frequencies, and phases of the GWs excited by plumes or clusters using the Boussinesq dispersion relation. In order to ensure that ω_{Ir} is compatible with the dispersion relation in the ray trace model, we assume that the calculated amplitude is correct for a given GW with (k, l, m), and recalculate the GW's intrinsic frequency using the high-frequency anelastic GW dispersion relation [*Vadas and Fritts*, 2009]:

$$\omega_{Ir}^2 = \frac{k_H^2 N^2}{m^2 + k_H^2 + 1/4H^2}, \tag{4}$$

where H is the density scale height [*Gossard and Hooke*, 1975; *Marks and Eckermann*, 1995]. This dispersion relation implies

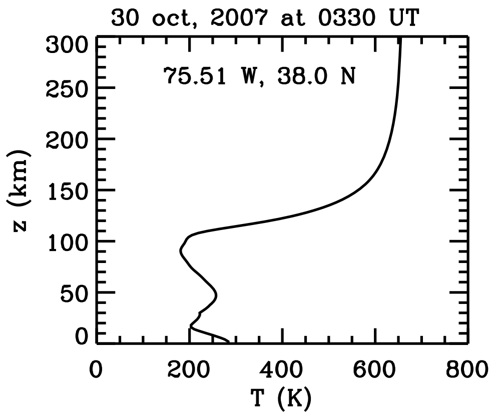

Figure 1. Temperature at 75.51°W and 38°N on 30 October 2007, at 0330 UT.

an observed horizontal GW phase speed in the direction of GW propagation of

$$c_H = \frac{\omega_r}{k_H} = \frac{N}{\sqrt{m^2 + k_H^2 + 1/4H^2}} + U_H. \quad (5)$$

[10] We now also include the effects of parameterized wave breaking from self and wave-wave interactions via the use of Lindzen's saturation condition [*Lindzen*, 1981], as it is now known to be important in the thermosphere for large-amplitude waves [*Yiğit et al.*, 2008, 2009; D. C. Fritts, personal communication, 2010]. Without this effect, the non-dimensional wave amplitudes in this study would have been ~5–20, implying wave breaking at lower altitudes [*Fritts and Alexander*, 2003]. These large amplitudes occur because we are simulating many clusters with large updraft velocities here. Including this effect decreases the altitude where the thermospheric body forces are maximum. In order to include this effect, we first ray trace the GWs from each convective object, reconstruct the GW solution, and add this solution to the total GW solution. We also calculate the sum of the non-dimensional amplitudes squared in each (x, y, z, t) bin. We then run the ray trace model for all convective objects again, and reduce the amplitude of each GW as needed so that the summed non-dimensional amplitude equals one [*Smith et al.*, 1987]. This reduces the wave amplitudes, and alters the background flow via the deposition of momentum. We only include this effect for the forward ray tracing simulations in section 3. Thus, the body forces we calculate are due to kinematic viscosity, thermal diffusivity, and parameterized GW breaking.

[11] For the reverse ray trace studies shown in section 5, we do not include any wave dissipation (i.e., we set $\mu = 0$). We do this for the following reasons. First, the model background thermospheric winds are likely different from the actual background winds. This causes the ray-traced GWs to dissipate at different altitudes than in the real atmosphere. For example, if the actual winds are stronger in the south(S)ward direction, then Nward-propagating GWs might have intrinsic frequencies closer to the buoyancy frequency, thereby allowing for deeper penetration into the thermosphere than "predicted" by the model winds. This background wind uncertainty (which yields an uncertainty in ω_{Ir}) is quite significant when ray tracing above $z = 200$ km, especially during solar minimum. Second, λ_z must be known in order to reverse ray trace a GW. When dissipation is unimportant, there is only 1 negative m solution for an upward-propagating GW [*Marks and Eckermann*, 1995]. However, where dissipation is important in the thermosphere, there are typically many negative m solutions at each altitude for an upward-propagating GW. This can be seen in the negative m portion of Figure 1 in *Vadas and Nicolls* [2009]. These curves are quite sensitive to the background winds. For these reasons, we do not reverse ray trace the observed GWs with dissipation. The assumption of zero dissipation implies that the difference in the horizontal distance traveled near the dissipation altitude is small. We will show this to be the case for GWs with $\lambda_z \ll 4\pi H$ (near the dissipation altitude) in section 5.4.

[12] The horizontal wind and temperature models we employ for ray tracing depend on x, y, z, and t. They include data from balloon soundings below ~30 km at Miami, Florida at 0 UT on 30 October 2007, and include data from the 3D Thermosphere-Ionosphere-Mesosphere-Electrodynamics General Circulation Model (TIME-GCM) from 35 km to ~500 km with 5° horizontal resolution. The TIME-GCM predicts the winds, temperatures, major and minor composition, and electrodynamic quantities globally [*Roble and Ridley*, 1994]. The inputs required by the TIME-GCM include the solar flux, auroral particle precipitation, high latitude electric fields, and tides propagating up from below the 10 mb lower boundary [e.g., *Crowley et al.*, 2006a, 2006b]. The model run performed for this study is described in detail by G. Crowley et al. (manuscript in preparation, 2010). The model was driven by high latitude inputs specified by the Assimilative Mapping of Ionospheric Electrodynamics (AMIE) algorithm [*Kamide and Richmond*, 1982; *Richmond and Kamide*, 1988; *Richmond*, 1992]. The TIME-GCM was driven by F10.7 fluxes using the EUVAC model [*Richards et al.*, 1994]. The tidal inputs are monthly climatological tides [*Hagan et al.*, 1999]. Because it is a climatology model, it does not include the day-to-day variability in the winds. Because it is not high resolution, it may not capture some of the large wind variations in the lower thermosphere that are better simulated by the high resolution TIME-GCM [*Larsen and Fesen*, 2009]. We discuss how possible wind errors affect our results later.

[13] Figure 1 shows the temperature profile, $\overline{T}$, over Wallops Island at 0330 UT on 30 October 2007. The thermospheric temperature is very low, $\overline{T} \sim 650$ K. Figure 2 shows the zonal and meridional winds from the TIME-GCM on 29 and 30 October at $z = 150$ and 200 km at Wallops Island. Dotted lines indicate the time interval for the TIDDBIT data. We clearly see the diurnal tidal component of the neutral wind. At $z = 200$ km, the winds are southeast(SE) prior to and during the analysis window. This suggests that the primary GWs which survive dissipative filtering will be propagating NW, N, and NEward [*Fritts and Vadas*, 2008]. Figure 3 shows hodographs of the winds at the location of and SE of Wallops Island at 0330 UT. These locations show the background winds encountered by some of the GWs excited by TS Noel. The winds are small, have significant latitudinal variations, and mostly rotate clockwise with altitude at this northern latitude location. At $z \sim 200$ km, the winds are SE or Sward at these locations.

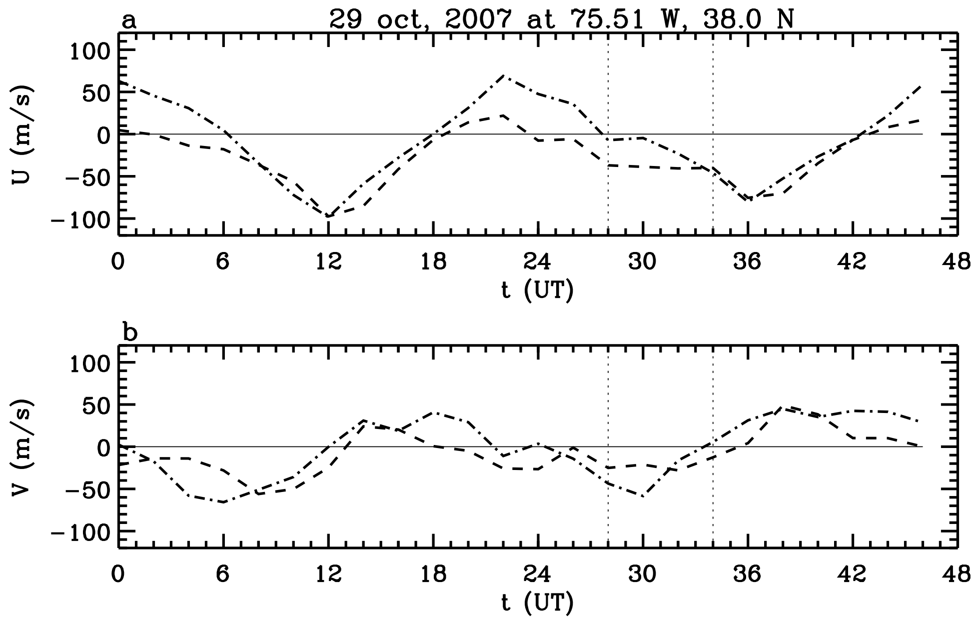

Figure 2. (a) Zonal and (b) meridional background winds at 75.51°W and 38°N on 29–30 October 2007. The dashed lines show z = 150 km, and the dash-dotted lines show z = 200 km. The dotted lines show 0400 and 1000 UT on 30 October.

Note that at $z \sim 240$ km, the winds are SEward at Wallops Island.

3. Excitation, Propagation, and Dissipation of Convective GWs From TS Noel

[14] In this section, we calculate the locations of the mesospheric and thermospheric body forces which result from the saturation and dissipation of the small and medium-scale primary GWs excited by TS Noel. These calculations are crucial in order to determine the identities and source locations of the TIDDBIT waves in section 5.

3.1. Temperature-Colored Satellite Image

[15] Figure 4 shows a GOES satellite image of eastern North America at 0432 UT on 30 October 2007. Wallops Island is shown as a red star. This image is dominated by TS Noel centered near 73°W and 22°N. Noel started as a tropical depression on 28 October at 0 UT, was upgraded to a TS on 28 October at 1200 UT, and was further upgraded to a hurricane on 02 November at 0 UT. When upgraded to a hurricane, Noel was located at 77°W and 26°N. By 0 UT on 03 November, it began to dissipate as it reached the cold water off the eastern coast of North America at 72°W and 32°N. It subsequently moved NEwards up the east coast of

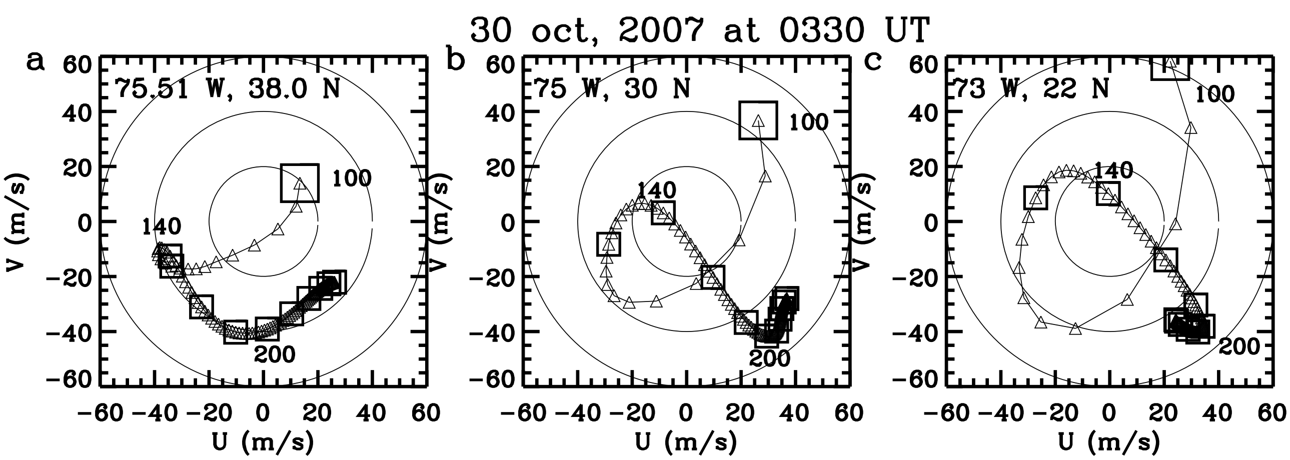

Figure 3. Hodograph of the background horizontal wind from z = 100 to 300 km at 0330 UT from the TIME-GCM. (a) 75.51°W and 38.0°N. (b) 75°W and 30°N. (c) 73°W and 22°N. The large square denotes the wind at z = 100 km, the triangles are every 2 km, and the medium squares are every 20 km. The labels “100”, “140”, and “200” indicate altitudes (in km).

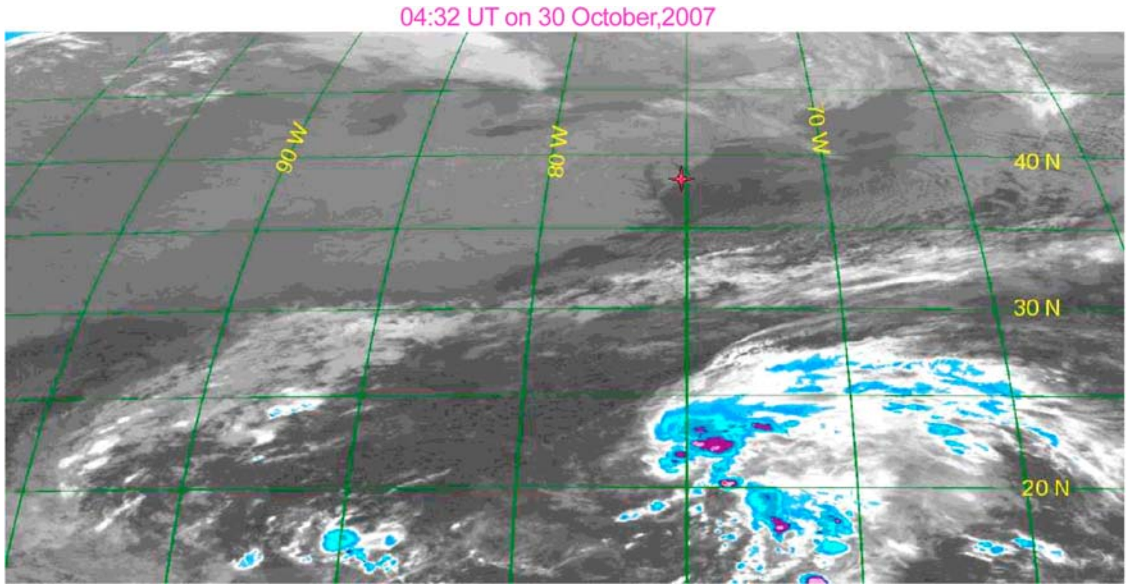

Figure 4. Satellite image on October 30 at 0432 UT. The transition from white to blue occurs at −55°C. The temperature is shown in 5°C intervals for colder temperatures. The dark purple color denotes −75 to −80°C. The plum and red colors denote fluid colder than −80°C. Wallops Island is shown by the red 4-pointed star.

North America, and dissipated by 06 November at 0600 UT near 50°W and 64.2°N.

[16] Figure 4 is colored by temperature. This is important, because it allows for identification of the plumes and clusters undergoing convective overshoot. From balloon soundings and the National Centers for Environmental Prediction (NCEP) reanalysis data, we estimate a tropopause temperature of ~ −79°C at $z_{\rm trop}$ = 15.0 ± 0.5 km. Localized cold temperatures on the anvils imply convective overshoot, because a parcel of air which moves adiabatically through the tropopause and into the stratosphere has a colder temperature than the surrounding air. Therefore, the plum and red colors in Figure 4 (which denote fluids colder than −80°C) are indicative of regions where convective overshoot occurred. We see that convective overshoot occurred near and SE of the center of TS Noel. Additionally, there is a single plume undergoing convective overshoot in the Carribbean Sea just east of the Yucatan Peninsula.

[17] The band of white clouds noticeable between Noel and the east coast of the United States is an area of weak convection and high cirrus clouds. These cloud tops were much warmer than the tropopause (white regions denote temperatures of $\overline{T} > -55$°C); therefore, they were located well below the tropopause. Note that Bermuda (65°W and 32°N) was reporting towering cumulous at the time, which is convection that has not grown into thunderstorms which reach the tropopause. Figure 5a shows a balloon sounding at Bermuda taken at 00 UT on 30 October 2007, which is a higher resolution depiction of the atmospheric stability occurring in this area. Bermuda was somewhat south of a cold front, which provided mechanical lift to low level air parcels. An air parcel rises along a moist adiabat (parallel to the green line), and has buoyancy until reaching a temperature equal to the observed temperature (red line), which occurs at $z \sim 9.3$ km. Above this altitude, momentum carries the parcel a few hundred meters until it cools and sinks below this altitude. Then it warms and rises, etc. The parcel thus oscillates around this equilibrium level. At this latitude, the tropopause is ~12.5–13 km. Therefore, it is unlikely that the weak convection occurring in these white bands of clouds excited any high-frequency GWs, because the convection never reached the tropopause.

[18] Figures 5b and 5c show the zonal and meridional winds from this balloon sounding. We see that there is a strong zonal shear at this location. This wind shear could have generated GWs if unstable to the Kelvin-Helmholtz instability [*Fritts*, 1982]. These GWs would have had phase speeds comparable to the mean wind, ~20–30 m/s, and horizontal wavelengths of a few to tens of km (*Fritts and Alexander*, 2003). Because only GWs with $c_H > 100$ m/s can propagate to the bottomside of the F layer (V07), and the observed waves have $c_H \geq 140$ m/s and $\lambda_H > 100$ km (see section 4.2), it is quite unlikely that any of the TIDDBIT waves were generated by an unstable tropospheric shear.

3.2. Convective Overshoot of Deep Plumes and Clusters

[19] Using Figure 4, we identify 15 convective objects which overshot the tropopause and likely excited primary GWs at 0432 UT. Figure 6 is a sketch showing the locations, types, horizontal diameters, and updraft velocities of these convective objects. The updraft velocities are obtained from the Convective Available Potential Energy (CAPE) maps [see *Vadas et al.*, 2009a]. TS Noel is an extremely energetic system, because (1) the most common convective object within it are clusters with plume diameters of $\mathcal{D}_{\rm H}$ = 10–20 km, and (2) the updraft velocities, $w_{\rm pl}$, are extremely large (up to $w_{\rm pl}$ = 75 m/s). Note that there are three extremely energetic clusters at 73–74°W and 22–23°N with $w_{\rm pl}$ = 65–75 m/s. Each convective plume/cluster typically lasts for 5–15 min before collapsing. Afterward, because potential energy is typically

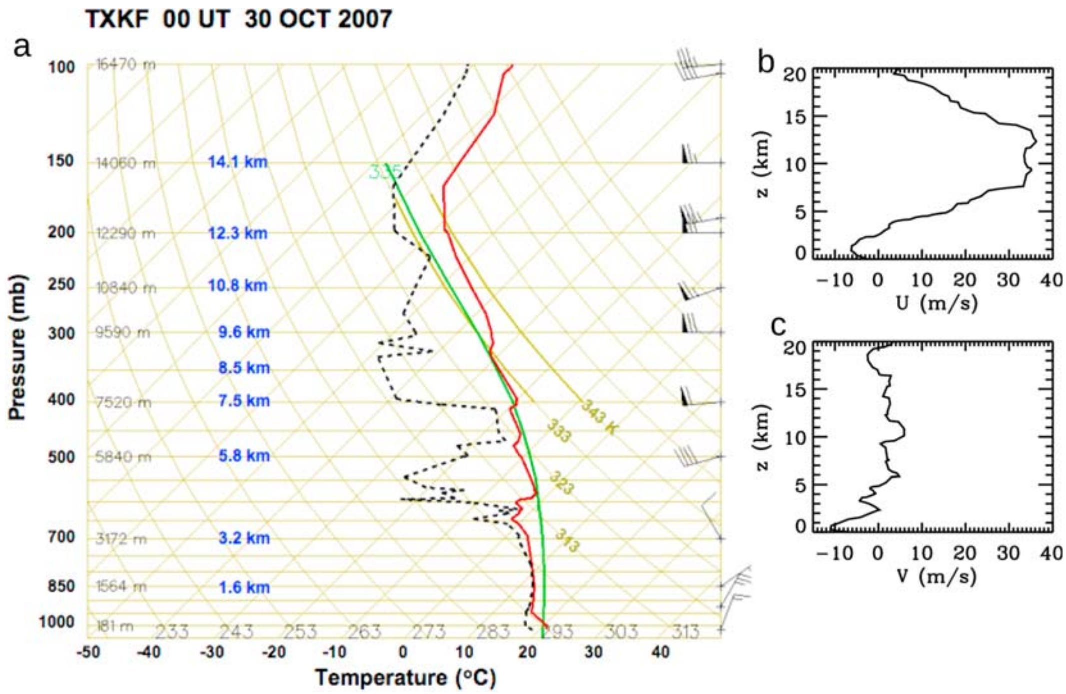

Figure 5. (a) Balloon sounding taken at Bermuda (TXKF: 32.37°N, 64.68°W) at 00 UT on 30 October 2007, plotted on a "Skew-T, log P" diagram. The vertical coordinate is the log of the pressure (in mb, black bold labels). The horizontal coordinate is temperature (°C, bold black labels), skewed so that the isotherms rise from lower left to upper right. Dry adiabats (°K, light black labels on x-axis, selected adiabats shown as gold labels) are the slightly curved lines sloping from lower right to upper left, and represent the rate of temperature change for a dry parcel rising or sinking adiabatically. The solid green line is a saturation adiabat (°K), which is the rate of temperature change for a rising/sinking moist parcel. The observed temperature is shown as a red line, and the observed dewpoints are shown as a dashed black line. The altitudes are shown in meters as light black labels on y-axis, and for selected heights in km as blue labels. (b) Zonal and (c) meridional winds from this sounding.

still available, another convective plume is formed near the outer edge of the original plume.

3.3. Propagation of Primary GWs

[20] We first calculate the GW spectra excited from the 15 convective objects shown in Figure 6. Examples of GW spectra from plumes and clusters are shown by *Vadas et al.* [2009a]. Next, we position each GW spectrum at the location of the convective object (at 0432 UT and $z = z_{\mathrm{trop}}$), and ray trace the GWs into the stratosphere, mesosphere, and thermosphere. Figure 7 shows horizontal slices of the reconstructed GW neutral density perturbations, $\rho'/\overline{\rho}$, from z = 100 to 220 km and from 0530 to 0630 UT. The times were chosen to show the evolution of the GW packet which contributes significantly to the creation of the thermospheric body force. The maximum amplitude for each image varies, and is as large as 30%. These GWs are saturated. Without the inclusion of wave saturation, the GW amplitudes would have been (unrealistically) 5–20 times larger; these values are much larger than in VL09 because (1) there are 15 convective objects here as opposed to a single convective plume, which greatly increases the wave amplitudes in regions of constructive interference, (2) most of the convective objects are clusters here, thereby increasing the GW amplitudes by a factor of ~2–3, and (3) the plume updraft velocities here are twice as large as in VL09, thereby doubling the GW amplitudes. These 3 effects yield GW amplitudes that are at least 8–12 times larger than in VL09 if wave saturation is not included. The maximum density perturbations of the primary GWs in VL09 was 10–15%. In hindsight, it was not necessary to include wave saturation in VL09, because nearly all of the primary GWs were unsaturated prior to dissipating from kinematic viscosity and thermal diffusivity.

[21] There are several important features in Figure 7. First, constructive and destructive interference of waves from different clusters and plumes is quite apparent. Second, the GWs at $z \geq 180$ km have $\lambda_H > 100$ km. This agrees with GW dissipative theory (V07). Third, the waves that survive to $z \sim 205$ km are propagating N, NW, NE, and Eward, but are not propagating S and SWward. This is because the winds are SWward at $z \sim 150$ km (see Figure 2). Finally, although the GWs appear as ~180–270° concentric rings at $z \leq 160$ km, they appear instead as partial "arcs" at $z \geq 175$ km because of dissipative filtering.

[22] Figure 8 shows horizontal slices of $\rho'/\overline{\rho}$ at $z = 140$ km from 0520 to 0700 UT. At early times, very large λ_H GWs are apparent. At later times, smaller λ_H GWs reach this altitude, since they have smaller vertical group velocities but similar periods. Figures 9a–9c shows $\rho'/\overline{\rho}$ at $z = 140$ km for

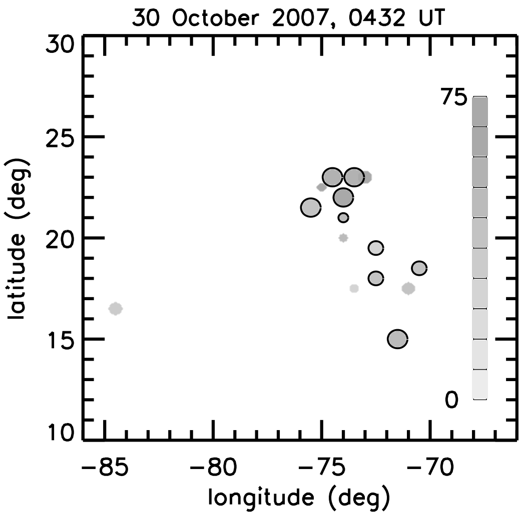

Figure 6. Sketch displaying the locations, updraft velocities, and types of the 15 convective objects from Figure 4. The center of each shaded circular region indicates the location of the convective object. The shading denotes w_{pl} on a linear scale from 0 to 75 m/s, as shown with the greyscale bar. Those shaded regions outlined by solid circles denote clusters. Those shaded regions with no outlines denote single plumes. The diameter of each shaded region, D, is linearly proportional to the diameter of each plume in the convective object, and is exaggerated by a factor of 5 for illustration purposes: D = $5\mathcal{D}_H$. For example, even though the single plume at 84.5°W and 16.5°N has an actual diameter of $\mathcal{D}_H$ = 15 km, it is pictured with a diameter of D = 75 km in the figure.

the most energetic cluster, the three most energetic clusters, and all 15 of the clusters and plumes. Although the most energetic cluster is visible in all panels of Figure 9, the other clusters and plumes contribute significantly in Figures 9b and 9c, creating complex interference patterns in Figure 9c. Note that the maximum amplitudes in Figures 9a–9c are similar because the waves are saturated (to different extents) in each panel.

3.4. Dissipation of Primary GWs and Creation of Horizontal Body Forces

[23] GWs transport momentum. Thus, when they break or dissipate in the atmosphere, they create horizontal body forces [*Hines*, 1972; *Vadas and Fritts*, 2004, 2006]. We now calculate the mesospheric and thermospheric body forces created from the breaking and dissipation of the primary GWs (e.g., Figure 7). The zonal and meridional components of the body force are

$$
\begin{aligned}
F_x &= -\frac{1}{\bar{\rho}}\frac{\partial\left(\bar{\rho}\overline{uw^*}\right)}{\partial z} \\
F_y &= -\frac{1}{\bar{\rho}}\frac{\partial\left(\bar{\rho}\overline{vw^*}\right)}{\partial z},
\end{aligned}
\tag{6}
$$

respectively [*Andrews et al.*, 1987]. Here, u, v, and w are the zonal, meridional, and vertical velocity perturbations of the GW, and overlines denote averages over 1–2 wave periods and wavelengths.

[24] Figure 10 shows the zonal and meridional components of the body forces at the latitudes where they are maximum. The meridional component is somewhat larger than the zonal component, and has a maximum value of $F_y \sim 0.85$ m s^{-2} (Nward) at 73.5°W, 24.4°N and z = 112 km. The zonal component maximizes at a somewhat higher altitude, z = 136 km, with a value of $F_x \sim 0.60$ m s^{-2} (Eward) at 71.7°W and 21.7°N. These accelerations are consistent with previous results from a single convective plume (VL09). However, the thermospheric body force is lower here by ~50–70 km because of wave saturation. Note that there is significant forcing up to $z \sim$ 190–200 km. The altitude of the body force maximum moves upwards in time.

[25] Both the zonal and meridional body force components excite secondary GWs [e.g., *Vadas and Fritts*, 2001]. We now focus only on the meridional body force component because (1) its amplitude is somewhat larger than the zonal component's amplitude, and (2) Nward-propagating secondary GWs at Wallops Island would be primarily created from the meridional component of the force, because horizontal body forces do not excite significant secondary GWs perpendicular to their direction of action. Figure 11 shows horizontal slices of F_y as a function of time. The contour levels in the first row (near the mesopause) are 10 times smaller than in rows 2–5. The mesospheric body forces (at $z \simeq 90$ km) are located north of the deep convective clusters, but end abruptly at 26–27°N. On the other hand, although F_y is maximum in the thermosphere at 24.4°N, there are significant large-amplitude thermospheric body forces up to ~33°N, especially for late times at z = 160 to 180 km. Thus, the horizontal regions covered by the mesospheric and thermospheric body forces are quite different. This occurs because different waves (with different λ_H and c_H) contribute at each altitude and location. In particular, the waves which contribute most strongly to the mesospheric body force have $\lambda_H \sim$ 20–30 km (and small c_H), whereas the waves which contribute most strongly to the thermospheric body force have $40 < \lambda_H < 150$ km (and larger c_H) (VL09). We now investigate why the breaking/dissipating GWs propagate to ~35°N at $z \sim$ 160–180 km, but propagate only as far north as ~27°N at $z \sim$ 90 km.

[26] A Boussinesq GW in a windless, isothermal atmosphere propagates at the angle α with respect to the vertical via [*Kundu*, 1990]

$$\cos\alpha = \tau_b/\tau_r, \tag{7}$$

where $\tau_b = 2\pi/N$ is the buoyancy period. Therefore, smaller period waves propagate closer to the vertical than larger period waves. When a GW propagates vertically by Δz, it also propagates horizontally, Δx_H, during the same time by

$$\Delta x_H \sim c_{g,H}\Delta t \sim \left(c_{g,H}/c_{g,z}\right)\Delta z, \tag{8}$$

where $c_{g,H} = \partial\omega_{Ir}/\partial k_H$ and $c_{g,z} = \partial\omega_{Ir}/\partial m$ are the horizontal and vertical group velocities, respectively, and Δt is the time taken to propagate Δz and Δx_H. Since $c_{g,H}/c_{g,z} \sim m/k_H \sim \tau_r/\tau_b$ from equation (1), equation (8) becomes

$$\Delta x_H \sim \Delta z\tau_r/\tau_b. \tag{9}$$

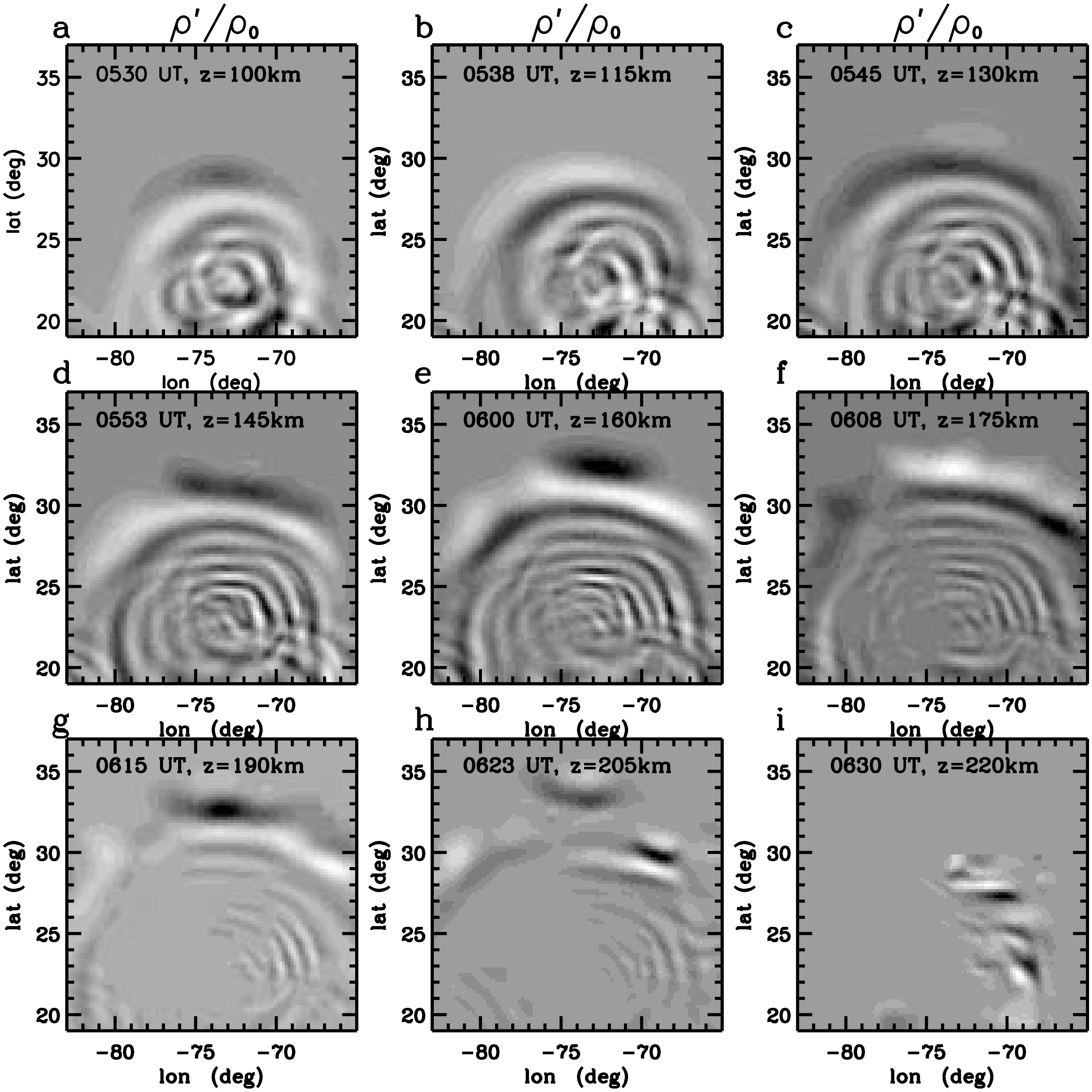

Figure 7. Horizontal slices of $\rho'/\overline{\rho}$ every 15 km from z = 100 to 220 km, and every 7.5 min from 0530 to 0630 UT, as labeled. Maximum positive values are white, and maximum negative values are black. The maximum values of $|\rho'/\overline{\rho}|$ are (a–c) 20, 24, and 22%; (d–f) 21, 23, and 29%; and (g–i) 18, 3, and 2 × 10^{-3}%.

Equation (9) shows the well-known result that GWs with larger periods travel further horizontally than GWs with smaller periods while propagating the same vertical distance Δz [e.g., *Hines*, 1967; *Richmond*, 1978; *Waldock and Jones*, 1987; V07].

[27] For a GW to propagate from 23°N to at least 27°N from the tropopause to z = 90 km, it needs to have a period of $\tau_r \geq 32$ min from equation (9), where $\Delta z \sim 90–15 = 75$ km and $\tau_b \sim 5.5$ min. Since the meridional component of the phase speed is

$$c_y = \omega_r/l = \lambda_y/\tau_r, \tag{10}$$

those Nward GWs having $\lambda_y \leq 30$ km will have phase speeds of $c_y \leq 15$ m/s. Because the model winds are $V \sim 10$–15 m/s at $z \sim 70$–80 km, all of those GWs with $\lambda_y \sim 20$–30 km and $\tau_r \geq 32$ min are removed by critical level filtering. Waves with shorter periods have larger $c_y = \omega_r/l$ (thereby avoiding critical levels), and reach $z \simeq 90$ km south of 27°N, where they break and contribute to the mesospheric body force. On the other hand, a medium-scale Nward GW with $\lambda_y \sim 100$ km can propagate from 23°N to 33°N from the tropopause to z = 160 km with a period of $\tau_r \simeq 45$ min from equation (9), where we have taken $\tau_b \sim 6$ min. From equation (10), those Nward GWs having $\lambda_y \sim 100$ km and

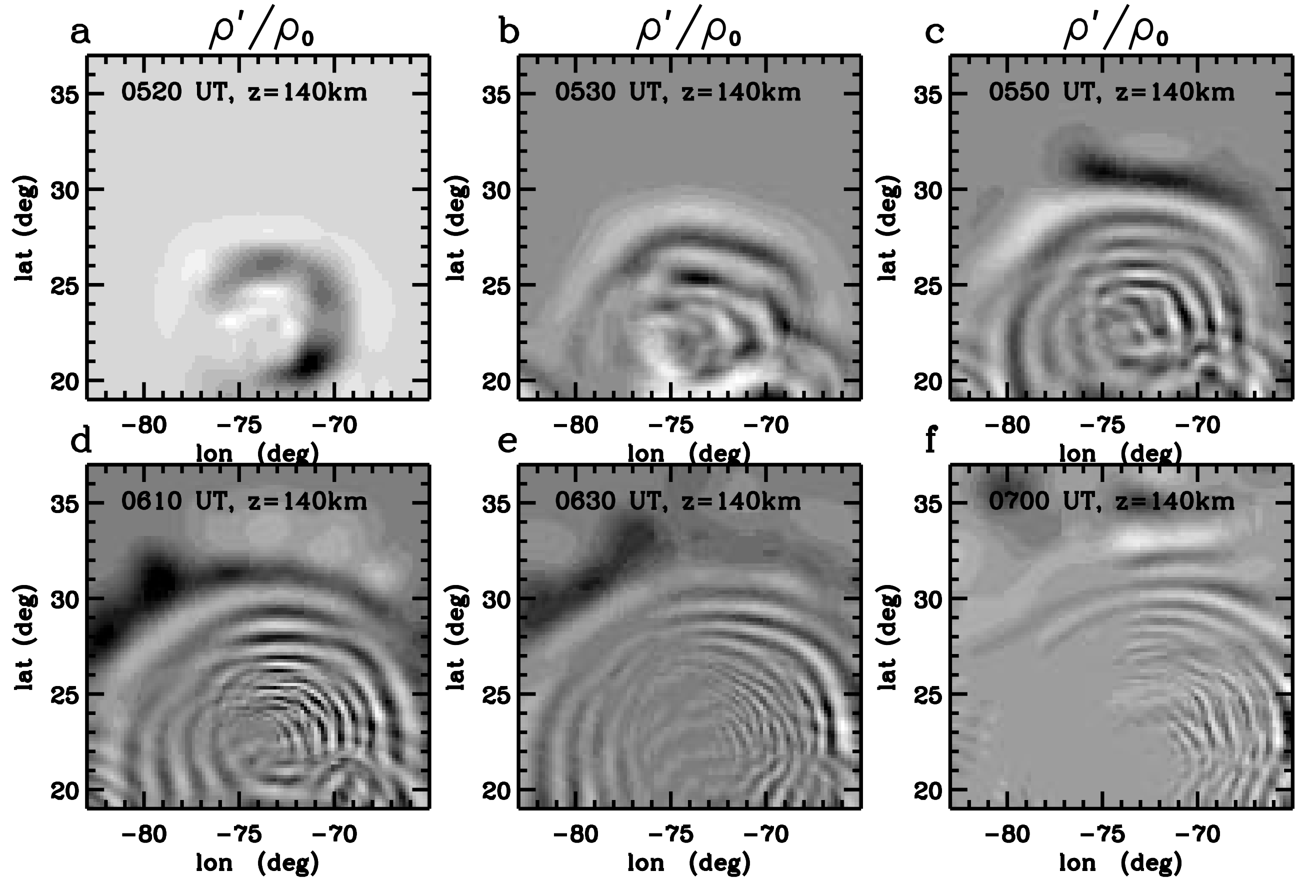

Figure 8. Horizontal slices of $\rho'/\overline{\rho}$ at z = 140 km at 0520, 0530, 0550, 0610, 0630, and 0700 UT, as labeled. The maximum values of $|\rho'/\overline{\rho}|$ are (a–c) 34, 18, and 23% and (d–f) 23, 23, and 17%.

$\tau_r \simeq$ 45 min have phase speeds of $c_y \simeq$ 40 m/s. Thus, these latter GWs escape critical level filtering in the lower atmosphere. Once in the thermosphere, these GWs avoid critical level filtering because the winds are generally Sward or slightly Nward (see Figure 3); eventually, they dissipate. Therefore, it is the larger phase speeds of the GWs which dissipate at $z \sim$ 160 km as compared to those which dissipate at $z \sim$ 90 km that leads to the thermospheric body forces extending much further north than the mesospheric body forces in Figure 11.

[28] We note from Figure 11 that the spatial inhomogeneities of the thermospheric body forces, ~100–150 km, are

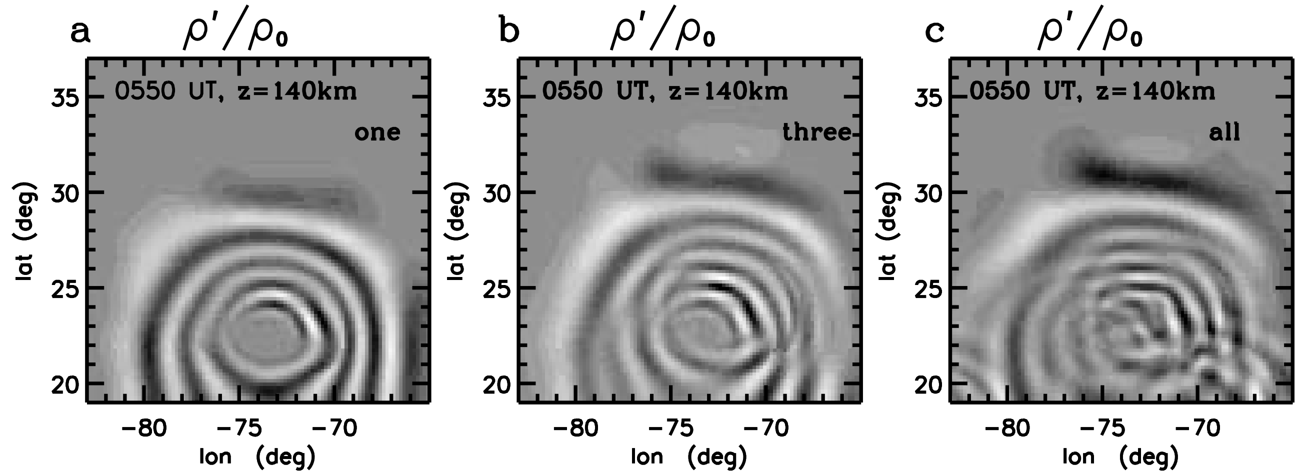

Figure 9. Horizontal slices of $\rho'/\overline{\rho}$ at z = 140 km at 0550 UT (a) for the cluster with the largest updraft velocity, (b) for the three clusters with the largest updraft velocities, and (c) for all 15 convective objects. The maximum values of $|\rho'/\overline{\rho}|$ in Figures 9a–9c are 14, 19, and 22%.

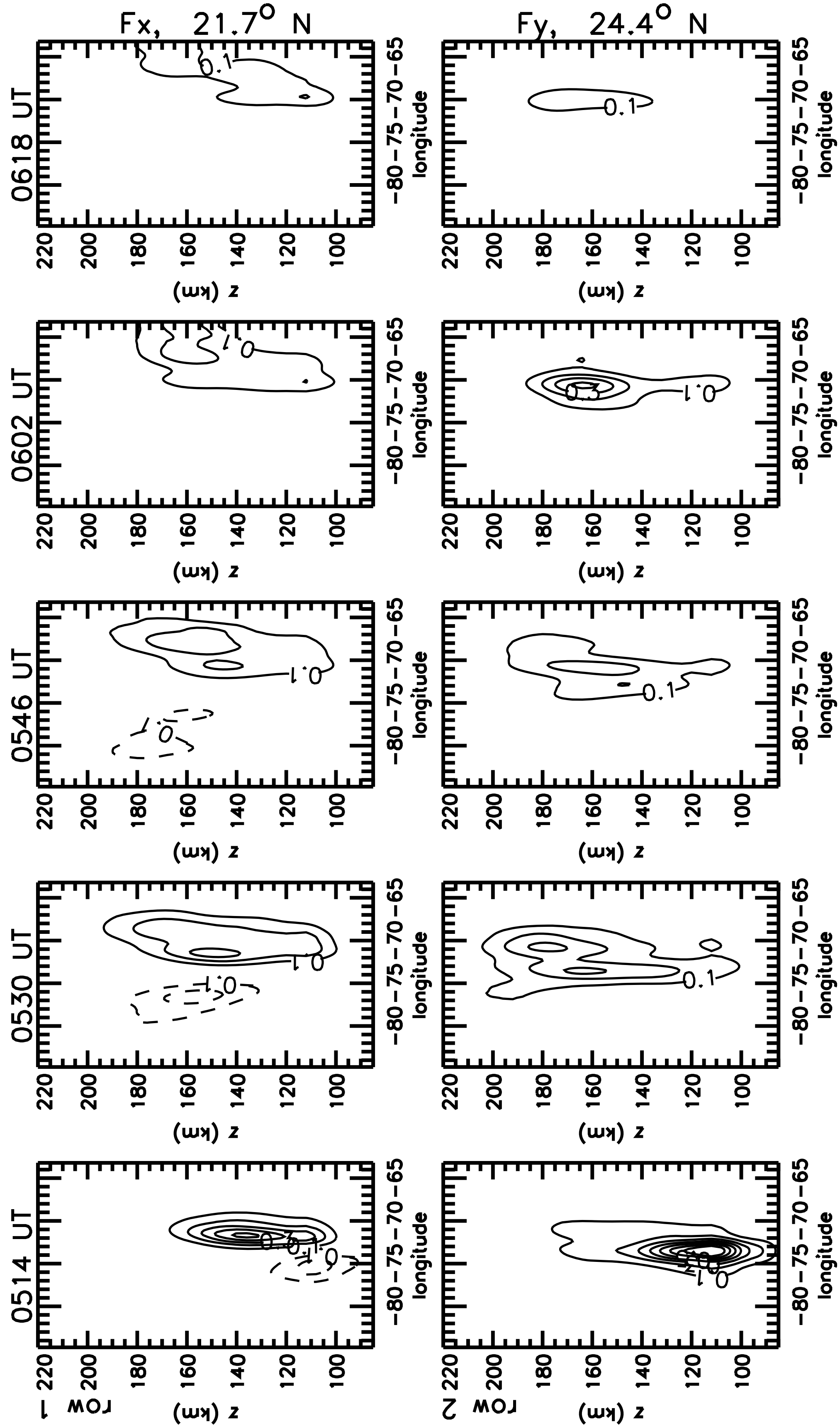

Figure 10. Body forces created from the dissipation of GWs excited from all 15 convective objects in intervals of 0.1 m s^{-2}. Solid lines indicate positive values, and dashed lines indicate negative values. (top) Zonal acceleration at 21.7°N. (bottom) Meridional acceleration at 24.4°N. The first through fifth times in each row correspond to 0514, 0530, 0546, 0602, and 0618 UT, respectively.

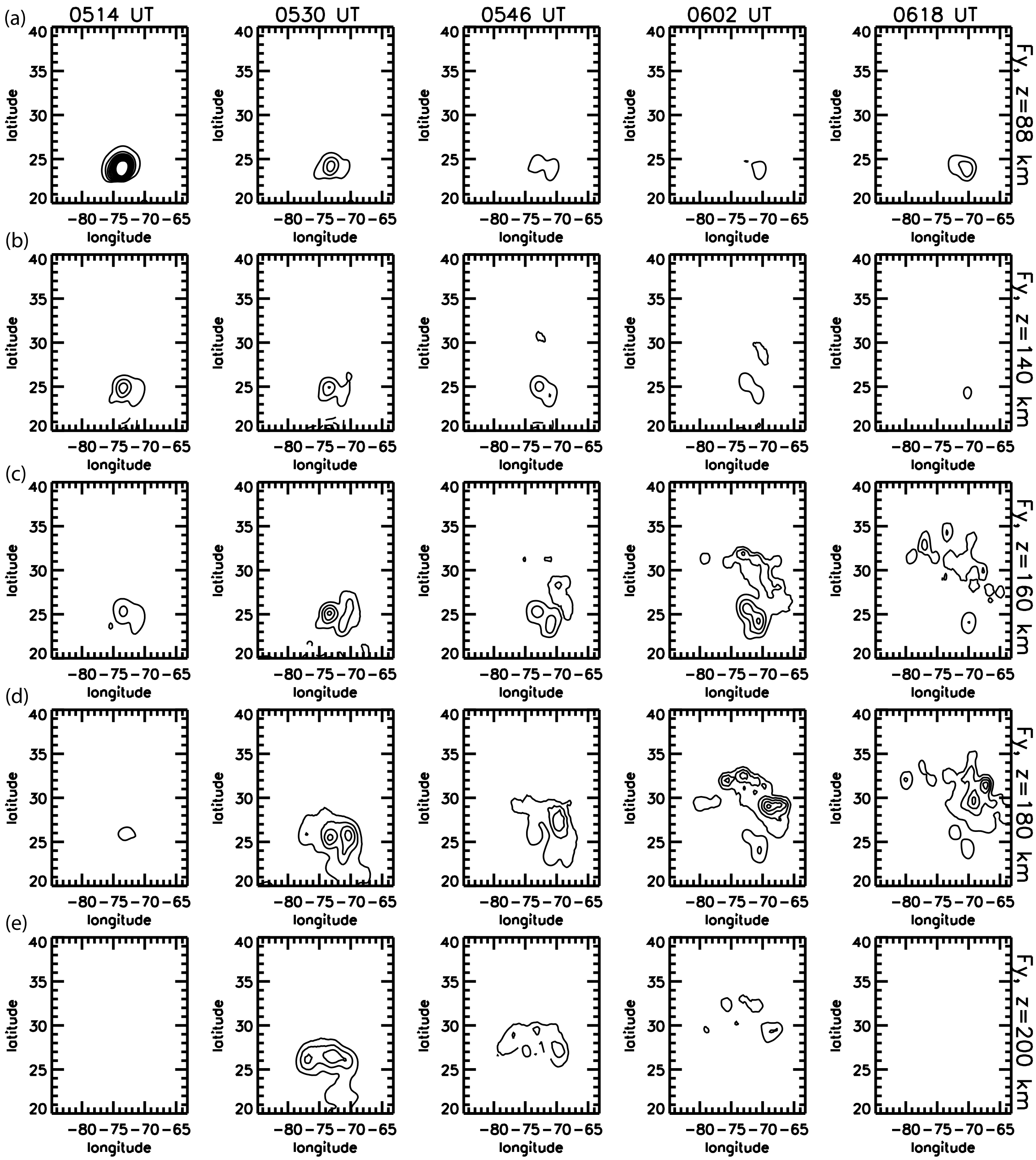

Figure 11. F_y as a function of longitude and latitude in intervals of (a) 0.01 m s^{-2} and (b–e) 0.1 m s^{-2}. Solid lines indicate positive values, and dashed lines indicate negative values. The first, second, third, fourth, and fifth times in each row correspond to 0514, 0530, 0546, 0602, and 0618 UT, respectively. Figures 11a–11e show z = 88, 140, 160, 180, and 200 km, respectively.

much smaller-scale than that calculated previously from a single plume [*Vadas and Fritts*, 2006, hereafter VF06; VL09]; this occurs because of constructive and destructive interference created by the GWs from the 15 convective objects. For z > 140 km, each image is different from the previous image, implying thermospheric body force durations of ≤15 min. These spatial inhomogeneities and temporal intermittencies imply excited secondary GWs from the thermospheric body forces with $\lambda_H \sim$ 100–400 km and $\tau_{Ir} = 2\pi/\omega_{Ir} \sim$ 10–20 min.

[29] Although we calculated the response from a single satellite image, because the storm was fairly uniform in time and slow-moving, it is likely that the spatial variability of the body forces during this 6-hr period can be approximated

as averages in time of Figure 11. The temporal variability is still ≤15 min, because of the variability of the exact plume and cluster locations and times.

[30] Summarizing, the approximate region occupied by the mesospheric body forces at z = 90 km is 69–78°W and 20–26°N, and the approximate region occupied by the thermospheric body forces is z = 110–190 km, 62–80°W and 20–33°N. Portions of these regions will excite secondary GWs at various times. We choose z = 90 km and z = 140 km as the average mesospheric and thermospheric body force excitation altitudes, respectively, for purposes of reverse ray tracing the TIDDBIT waves in section 5.

4. TIDs Observed by TIDDBIT Near Wallops Island

4.1. TIDDBIT Ionospheric Sounder

[31] The TIDDBIT sounder was installed in the Wallops Island region, and collected ~30 days of data before the rocket launch, and seven days afterward. The system is described in detail by G. Crowley and F. Rodrigues (Characteristics of traveling ionospheric disturbances observed by the TIDDBIT sounder, manuscript in preparation, 2010), and G. Crowley et al. (manuscript in preparation, 2010). Similar systems have been deployed in the past [e.g., *Crowley et al.*, 1987; *Crowley and McCrea*, 1988] but the new TIDDBIT data is completely digitized at the receiver, making data analysis much easier, and permitting large amounts of data to be conveniently analyzed. Briefly, the TIDDBIT ionospheric sounder utilizes three radio transmitters, separated by about 200 km in a triangular array, and one central receiver to measure TIDs propagating in the bottomside of the F region. The TIDs produce Doppler shifts in the three received signals. As the TIDs pass over the array, they perturb the Doppler shifts on each radio path at different times, and the time delays are determined by cross-spectral analysis for each wave period. Triangulation then yields the horizontal phase-trace velocities. Typically the data are analyzed in 3-hour windows to retain some level of stationarity in the signal, meaning the largest wave period resolved is 90 minutes. The data are sampled with a 30 second cadence; thus the TIDDBIT sounder provides a relatively complete picture of the TIDs, including the horizontal wavelength, phase speed, and propagation direction as a function of wave period from 1 min to 90 minutes.

[32] For this paper, we only discuss waves with periods greater than 15 min in order to exclude waves in the acoustic range: $15 \le \tau_r \le 90$ min. Quality control of the wave analysis is discussed by G. Crowley and F. Rodrigues (manuscript in preparation, 2010), and relies on the fact that the system uses two sounding frequencies to examine different heights, and the receiver collects and separates both magneto-ionic modes. Thus there are four independent measurements of the TID parameters. Typically, we require that TIDs must be detected with similar properties either in both the "o" and "x" modes, or on both frequencies.

4.2. Characteristics of the TIDs

[33] On 30 October from 0400-1000 UT, 59 TIDs were observed by the TIDDBIT system. The analysis windows were 0400-0700 UT, 0430-0730 UT, etc. The reflection (or observation) altitudes ranged from z_{obs} ~ 290 km at 0400 UT to z_{obs} = 235 km at 1000 UT. Figure 12 shows the attributes of these waves. Here, θ is the azimuth measured clockwise from north, and z_{obs} is the observation altitude. Note that the measured attributes of those waves with periods of $\tau_r \sim$ 90 min may have large uncertainties.

[34] Figure 12 shows that the waves have $c_H \ge 140$ m s^{-1} and $\lambda_H \ge 100$ km, in excellent agreement with GW dissipative theory [V07; *Fritts and Vadas*, 2008]. These waves spanned all azimuths except θ = 10–100°, although most (60%) were propagating NW/Nward (i.e., with $-58° \le \theta \le 5°$). Importantly, 24 (40%) of all TIDs and 10 (or 30%) of the NW/Nward TIDs have $c_H \ge 280$ m/s. We show now that if these waves are GWs, they could not have originated (or propagated) near the tropopause. From equation (5), the maximum phase speed a GW in the stratosphere can have is

$$\max(c_H) \simeq 2\mathrm{H}N + U_H. \tag{11}$$

Here we have set $\lambda_H \to \infty$ and $\lambda_z \to \infty$. Setting N = 0.02 rad/s and H $\simeq$ 7 km, equation (11) becomes max(c_H) ~ 280 ms^{-1} + U_H. From Figure 2, V is negative and is quite small (i.e., $|V| \le 20$ m/s). Therefore, the maximum horizontal phase speed of a Nward primary GW from deep convection (i.e., $U_H = V$) is

$$\max(c_H) \sim 280\mathrm{ms}^{-1}. \tag{12}$$

Note that the periods and phase speeds of the medium-scale TIDs (MSTIDs) in Figure 12 agree well with previous measurements of MSTIDs from convection (50 to 30 min and 100 to 300 m/s, respectively [*Rottger*, 1977].

[35] We also see in Figures 12f and 12h that τ_r is linearly proportional to λ_H. This is because λ_z is approximately constant within this limited altitude range, since λ_z increases nearly exponentially with altitude [*Oliver et al.*, 1997; *Djuth et al.*, 1997, 2004; V07]. Assuming negligible background winds and $m^2 \gg k_H^2$, equation (4) becomes

$$\omega_r \simeq k_H N / \sqrt{m^2 + 1/4\mathrm{H}^2}. \tag{13}$$

If $\lambda_z \ll 4\pi$H, then equation (13) becomes $\lambda_H \simeq \lambda_z \tau_r / \tau_b$. Then, τ_r is linearly proportional to λ_H if λ_z is relatively constant over the altitude range of interest. On the other hand, if $\lambda_z \gg 4\pi$H, then $\lambda_H \simeq 4\pi\mathrm{H}\tau_r/\tau_b$. Then, τ_r is linearly proportional to λ_H, because H and τ_b are approximately constant from z_{obs} = 240 to 290 km.

4.3. Comparison of TID Characteristics With GW Dissipative Theory

[36] Figure 13 shows histograms of the parameters of the TIDs propagating NW/Nward. The background climatology winds have been included here to calculate λ_z and τ_{Ir}. However, these results do not change substantially if the winds are zero instead (not shown). All of the GWs have $c_H \ge 140$ m s^{-1} and $\lambda_H \ge 100$ km, in excellent agreement with GW dissipative theory at these altitudes [V07; *Fritts and Vadas*, 2008]. Most of the GWs have $100 < \lambda_H < 500$ km, $100 < \lambda_z < 200$ km, $100 < c_H < 300$ m/s, and $10 < \tau_{Ir} < 20$ min. The narrow distribution in $\lambda_z \sim$ 100–200 km for $\lambda_z \ll 4\pi\mathrm{H} \simeq 380$ km agrees with GW dissipative theory (V07), and explains why τ_r is linearly proportional to λ_H in Figure 12h.

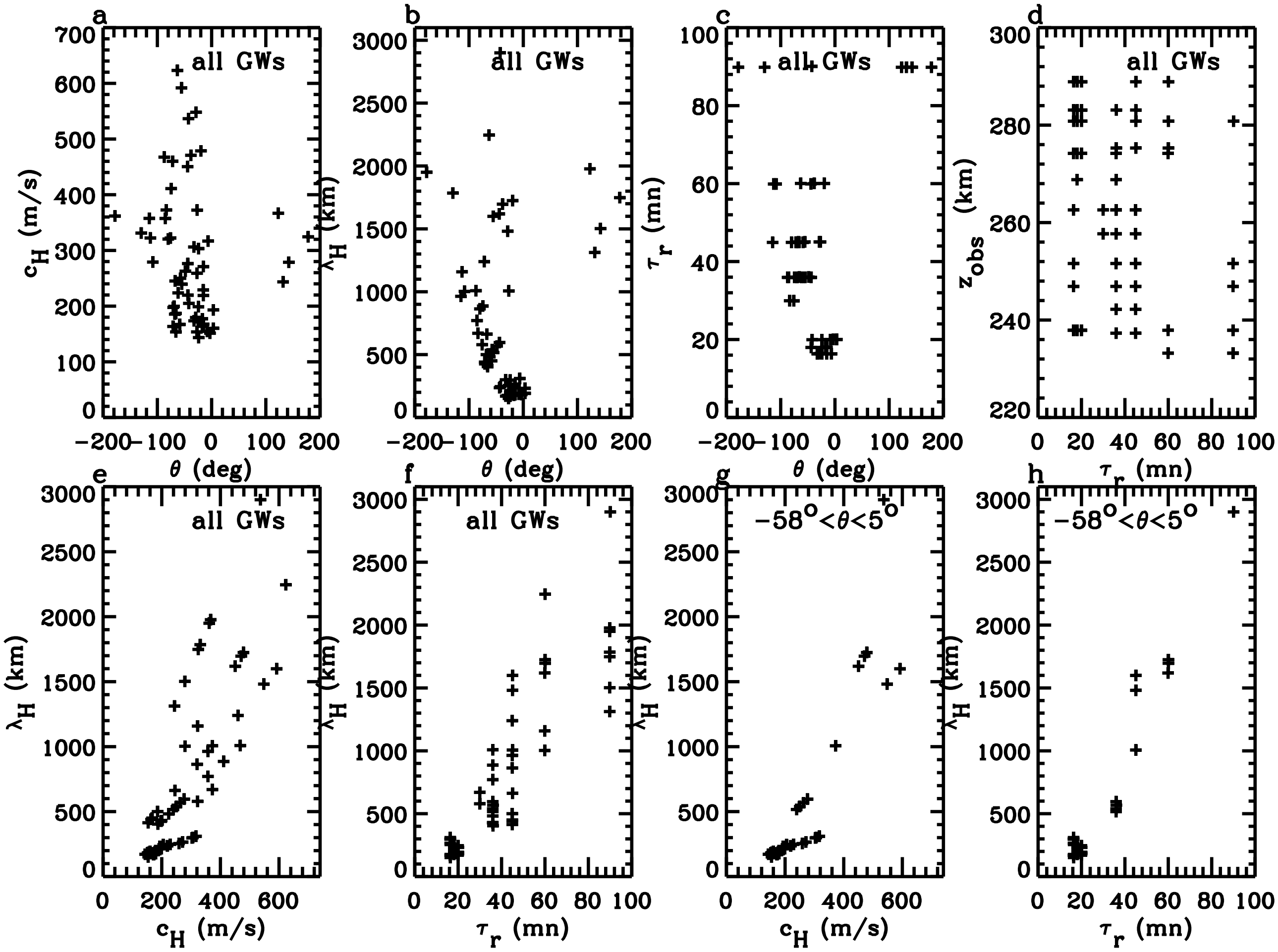

Figure 12. Attributes of the GWs observed by the TIDDBIT sounder from 0400-1000 UT on 30 October. Each "+" denotes a GW. (a–f) All 59 GWs. (g–h) Only those 33 GWs with azimuths of $-58° < \theta < 5°$. $\tau_r = 2\pi/\omega_r$ is the observed period, and z_{obs} is the observation altitude.

[37] A GW's momentum flux (per unit mass) is maximum at the "dissipation altitude", z_{diss}, given by equation (54) of VF05:

$$c_{g,z}/2\omega_{Ii} \sim \mathrm{H} \text{ at } z = z_{diss}. \quad (14)$$

Here, ω_{Ii} is the dissipative decay rate,

$$\omega_{Ii} = -\frac{\nu}{2}\left(\mathbf{k}^2 - \frac{1}{4\mathrm{H}^2}\right)\frac{[1 + (1 + 2\delta)/\mathrm{Pr}]}{(1 + \delta_+/2)}, \quad (15)$$

where $\mathbf{k}^2 = k_H^2 + m^2$, ν is the kinematic viscosity, $\delta = \nu m/\mathrm{H}\omega_{Ir}$, $\delta_+ = \delta\,(1 + \mathrm{Pr}^{-1})$, and Pr = 0.7 is the Prandtl number. We define the dissipation factor, ϵ, to be

$$\epsilon \equiv c_{g,z}/2\omega_{Ii}\mathrm{H}. \quad (16)$$

Then $\epsilon \simeq 1$ when a GW's momentum flux is maximum (i.e., at $z = z_{diss}$), $\epsilon \gg 1$ when a wave is not yet dissipating, and $\epsilon \ll 1$ when a wave is strongly dissipating. Thus, the value of ϵ is related to the amount of dissipation which a GW has undergone. Using $\delta \sim 0$ and equation (4) for weak dissipation, equation (16) becomes

$$\epsilon \simeq \frac{|k_H m| N}{\mathrm{H}\left(\mathbf{k}^2 + 1/4\mathrm{H}^2\right)^{3/2}\left|\mathbf{k}^2 - 1/4\mathrm{H}^2\right|\left(1 + \mathrm{Pr}^{-1}\right)\nu}. \quad (17)$$

Note that equation (17) agrees with *Vadas* [2007, equation (13)] for Pr = 1.

[38] We show ϵ at the observation altitudes in Figure 13f using μ as given by *Vadas* [2007, equation (2)]. The spectrum is broad, peaking at $\epsilon \simeq 0.1$. While many waves were moderately dissipating with $\epsilon \sim 1$, and others were strongly dissipating with $\epsilon \ll 1$, none of the waves were far below the dissipation altitude with $\epsilon \gg 1$. This agrees well with GW dissipative theory; from the top two rows of *Vadas* [2007, Figures 4 and 6], the highest attainable dissipation altitudes from launch altitudes of $z = 0$ and $z = 150$ km are $z_{diss} \sim$ 200–250 km and $z_{diss} \sim$ 225–300 km, respectively. Most of these altitudes are smaller or of order the observation altitudes. Therefore, the fact that we do not see GWs with $\epsilon \gg 1$ in Figure 13f agrees well with GW dissipative theory.

[39] The smallest value of ϵ in Figure 13f is given by $\log_{10}(\epsilon) \sim -1.8$. We now show that this also agrees well with GW dissipative theory. A GW can propagate (1–2)H above z_{diss} before its amplitude becomes negligible (V07). When a GW is 2H above z_{diss}, λ_z is approximately one-half as large as at z_{diss} when the thermospheric temperature is approximately constant (VF05). We assume that N and H are approximately constant over this altitude range, and

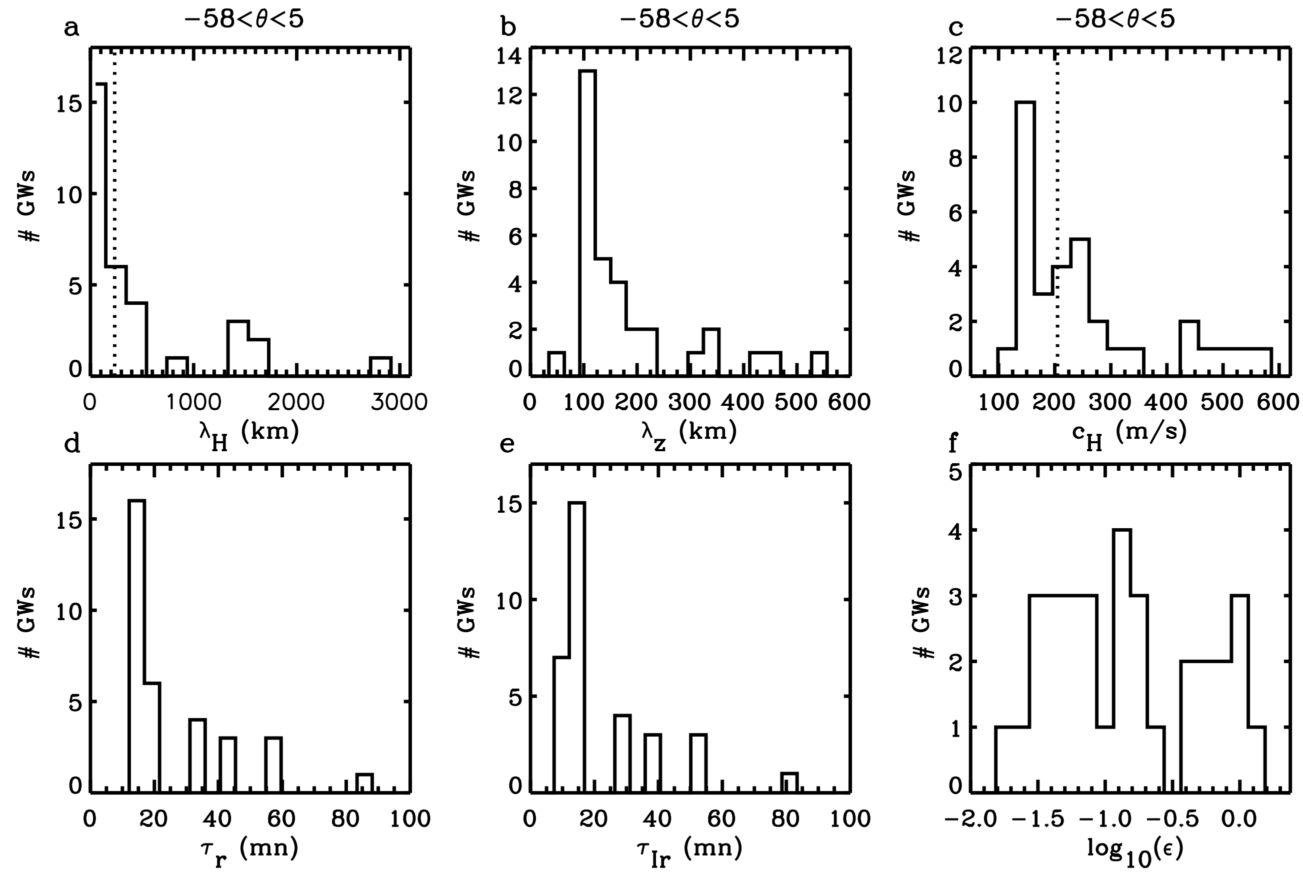

Figure 13. Histograms of the parameters of GWs with $-58° \leq \theta \leq 5°$. Here, ϵ is the dissipation factor, given by equation (17). The dotted lines show c_H = 205 m/s and λ_H = 235 km.

that $m^2 \gg k_H^2$ and $m^2 \gg 1/4\mathrm{H}^2$. Then, $\epsilon \propto m^{-4}\nu^{-1}$ from equation (17). Using $\nu(z) = \nu(z_{\rm diss})\exp((z - z_{\rm diss})/\mathrm{H})$,

$$\epsilon(z) = \epsilon(z_{\rm diss})\exp(-(z - z_{\rm diss})/\mathrm{H})\left[\frac{\lambda_z(z)}{\lambda_z(z_{\rm diss})}\right]^4. \quad (18)$$

Since $\epsilon(z_{\rm diss}) = 1$, the value of ϵ at $z = z_{\rm diss} + 2\mathrm{H}$ is then

$$\epsilon \simeq 2^{-4}\exp(-2) \sim 0.0085, \text{ or } \log_{10}(\epsilon) \simeq -2.1. \quad (19)$$

Therefore, GW dissipative theory predicts that all GWs with significant amplitudes have $\log_{10}(\epsilon) \geq -2.1$. This GW result agrees very well with Figure 13f.

[40] In conclusion, because the TID parameters agree very well with GW dissipative theory, we conclude that the TIDs observed by TIDDBIT were likely GWs. We therefore refer to these TIDs as GWs for the rest of this paper.

5. Tropospheric, Mesospheric, and Thermospheric Sources of GWs

[41] In this section, we compare the locations of the reverse ray traced GWs with the regions of (1) convective overshoot, (2) mesospheric body forces, and (3) thermospheric body forces. We allow those GWs which reflect near the ground or in the mesosphere/thermosphere to do so, in order to consider all possible sources for these waves. We note that GWs with relatively slow phase speeds thought to be excited from auroral heatings have been observed reflecting off the ground [e.g. *Samson et al.*, 1989, 1990; *Bristow et al.*, 1994]. Additionally, modeling has shown that fast-moving GWs reflect in the lower thermosphere (VL09).

5.1. Reverse Ray Trace Setup

[42] We now reverse ray-trace the observed GWs back to deep convective objects, to mesospheric body forces, and to thermospheric body forces, if possible. We assume that all of the GWs are upward-propagating at the time they are observed. Because the observation altitudes are z = 240–290 km, this is a good assumption, as there are no known significant wave sources above 300 km. For the convective overshoot source, we ray trace the GWs backwards in time to z = 16 km (if possible), which is $z_{\rm trop}$ + 1 km to allow for convective overshoot. For the mesospheric body force source, we ray trace the GWs backwards in time to an average altitude of z = 90 km (with and without reflection, if possible). For the thermospheric body force source, we ray trace the GWs backwards in time to an average altitude of z = 140 km (with and without reflection, if possible). Figure 14 shows a sketch of the geometry of these possible sources. The primary GWs are those excited directly by the deep convective plume (solid lines). Although both upward and downward propagating primary GWs are excited, there is negligible horizontal displacement for the high-frequency GWs we observe here; therefore, we only show the upward-propagating primary GWs here. The mesospheric and thermospheric horizontal

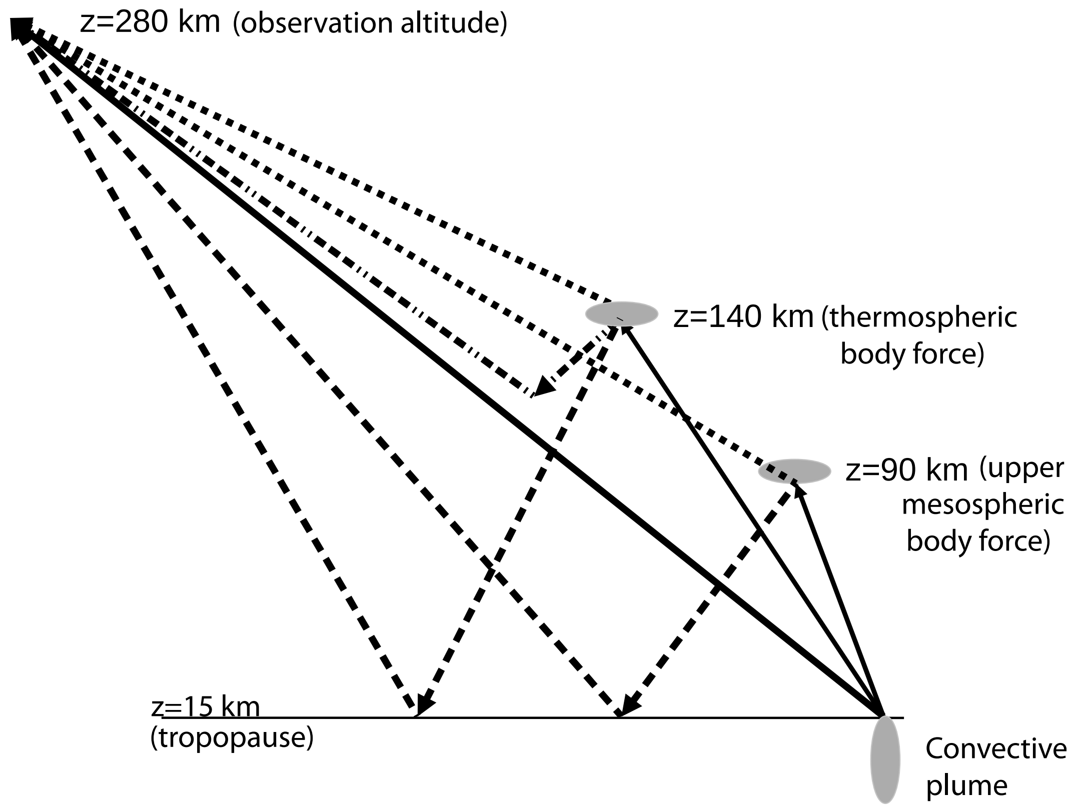

Figure 14. Sketch of the possible sources of GWs arising from a single deep convective plume. The convective plume excites primary GWs (solid lines). Those with large λ_z might be able to propagate to the observation altitude. Those with smaller λ_z dissipate at $z \sim 90$ km ($\lambda_H \sim 20$–30 km) and at $z \sim 140$ km ($\lambda_H \sim 50$–150 km), creating mesospheric and thermospheric horizontal body forces, respectively (grey ellipses). Each of these body forces excites a spectrum of upward (dotted lines) and downward (dashed and dashed-dotted lines) propagating secondary GWs. Those initially downward-propagating secondary GWs reflect upwards near the tropopause (dashed lines), or in the upper mesosphere/lower thermosphere (dashed-dotted lines).

body forces are created by the breaking and dissipation of primary GWs with $\lambda_H \sim 20$–30 km and $\lambda_H \sim 50$–150 km, respectively. Both upward and downward propagating secondary GWs are excited by these horizontal body forces. These GWs are called "secondary" because they are excited by a "secondary" process. The upward-propagating secondary GW are shown as dotted lines. The initially downward-propagating secondary GWs that reflect upwards at the tropopause are shown as dashed lines. Finally, an initially downward-propagating secondary GW from a thermospheric body force which reflects upward in the upper mesosphere/lower thermosphere is shown as a dash-dotted line.

5.2. Sources of All GWs

[43] Figure 15 shows the reverse ray-trace results for all 59 GWs. Figure 15 is nearly the same if the winds are assumed zero instead. Figures 15a and 15b shows the minimum altitudes attained by the GWs during reverse ray-tracing, $z_{\min}$. We see that there is a reasonably sharp transition between GWs which could have originated near the tropopause (i.e., $z_{\min} \leq 20$ km) and GWs that could not have originated near the tropopause (i.e., $z_{\min} \sim 80$–140 km). In particular, all of those GWs with $c_H < 200$ m/s could have been excited directly by deep convection, while most of those GWs with $c_H > 200$ m/s could not have been excited directly by deep convection. These latter waves must have instead been excited in the upper mesosphere or thermosphere. Note that those initially downward-propagating secondary GWs with $\lambda_H \sim 2000$–2500 km reflected upwards at $z \sim 110$–130 km, in agreement with the model results in VL09. We emphasize that for those waves with $z_{\min} < 20$ km, $z_{\min}$ may represent the source altitude for a primary GW (solid lines in Figure 14) or the reflection altitude for an initially downward-propagating secondary GW (dashed lines in Figure 14). Figure 15b shows that there are some larger-scale GWs with $\lambda_H \sim 400$–1100 that attain minimum altitudes of $z_{\min} < 20$ km, and therefore could have been generated by deep convection in principle; however, convection models do not predict the excitation of GWs with such large horizontal scales [*Vadas et al.*, 2009a].

[44] We now show the reverse ray trace results for these GWs. Figure 15c shows the locations of the GWs at $z = 140$ km if they are initially upward-propagating GWs. The diamond shows the location of Wallops Island. Some of these locations overlap well with the thermospheric body forces in Figure 11. Approximately 5–6 of these GWs seem to have originated above 50° geographic latitude, and may therefore have been launched by the northern aurora.

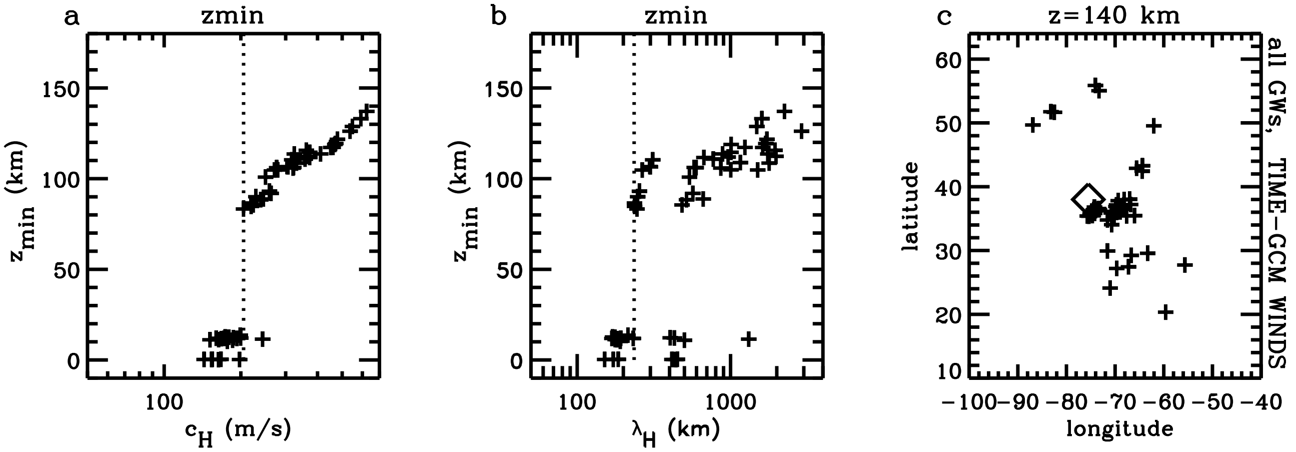

Figure 15. Reverse ray trace results using the model winds for all 59 GWs. (a) $z_{\min}$ as a function of c_H. The dotted line shows c_H = 205 m/s. (b) $z_{\min}$ as a function of λ_H. The dotted line shows λ_H = 235 km. (c) Locations of the GWs at z = 140 km (without reflection). The diamond shows Wallops Island.

5.3. Sources of Northwest/Northward Propagating GWs

[45] Figure 16 shows the reverse ray trace results for only those NW/Nward GWs (i.e., with $-58° \le \theta \le 5°$). Figures 16a and 16b shows that there is a sharp transition between those GWs which might be primary convective GWs and those GWs which could not. In particular, those GWs with $c_H <$ 205 m/s and λ_H < 235 km might have been generated directly by convective overshoot, whereas those GWs with c_H > 205 m/s and λ_H > 235 km could not have been generated from convective overshoot. Instead, these latter waves must have originated in the upper mesosphere or lower thermosphere. It is important to remember that although those GWs with c_H < 205 m/s and λ_H < 235 km might have been generated from deep convection, they might also have been generated as initially downward-propagating secondary GWs from mesospheric or thermospheric body forces, as mentioned previously.

[46] We first reverse ray trace the NW/Nward GWs with c_H < 205 m/s and λ_H < 235 km. We determine the locations of these waves at z = 140 km and at z = 90 km (not shown). These locations were too close to Wallops Island to overlap with either the mesospheric or thermospheric body forces. For example, the locations at z = 90 km were north of 32°N. We continue reverse ray tracing these waves. Figure 16c shows the GW locations at z = 16 km. We see that these locations occur at 28–33°N, which is ~500–1000 km north of any overshooting clusters/plumes in Figure 4. (Remember that the clouds between Noel and the east coast was an area of weak convection which likely did not generate high-frequency GWs.) Therefore, those NW/Nward GWs with c_H < 205 m/s and λ_H < 235 km were likely not primary convective waves. We will show why this makes sense in section 5.5.

[47] We continue reverse ray-tracing the GWs from Figure 16c backwards in time (with reflection at $z_{\min}$) to possible mesospheric and thermospheric body forces instead. Figure 16d shows the locations of the waves at z = 90 km. Three of these GW locations occur on the northern edge of the mesospheric body force source region in Figure 11. Figure 16e shows the GW locations at z = 140 km. These 11 GW locations occur at 62–80°W and 20–33°N, which overlaps with the thermospheric body force source region in Figure 11 extremely well. This includes the three waves which were located on the outside edge of the mesospheric body force in Figure 16d. We conclude that 11 of the NW/Nward GWs with c_H < 205 m/s and λ_H < 235 km were likely initially downward-propagating secondary GWs from thermospheric body forces created from TS Noel. Three of these waves may have instead been initially downward-propagating secondary GWs from mesospheric body forces created from TS Noel (see above), although this is much less likely. These secondary GWs were shown pictorally as dashed lines in Figure 14. We emphasize that because these GWs have c_H < 250 m/s, they were generally thought (perhaps incorrectly some of the time) to be excited near the tropopause in previous studies [see, *Hocke and Schlegel*, 1996].

[48] In Figures 16f–16h, we focus only on those waves with c_H > 205 m/s and λ_H > 235 km. Figure 16f shows the locations of the waves at z = 140 km if they are initially upward-propagating secondary GWs from thermospheric body forces. Those 6 waves with latitudes ≤33° and longitudes 62–80°W overlap well with the thermospheric body forces in Figure 11; therefore, we conclude that these 6 waves are likely initially upward-propagating secondary GWs from thermospheric body forces. (Note that because the "7th GW" at ~20°S and ~60°W is only slightly outside the thermospheric body force region, it might also have been excited by a thermospheric body force.) We continue reverse ray-tracing those GWs in Figure 16f backwards in time to z = 90 km. The locations are shown in Figure 16g. We see that few of these GWs even reach the mesopause, and those that do are too far north to be generated from mesospheric body forces. We therefore conclude that no initially upward-propagating GWs from mesospheric body forces were observed at Wallops Island by TIDDBIT.

[49] We continue reverse ray-tracing only those waves from Figure 16f that have latitudes >33°. (We are thus excluding the 7 GWs with latitudes <33° in Figure 16f, and are only ray tracing those GWs that are tightly clumped near Wallops Island in Figure 16f.) We allow these waves to

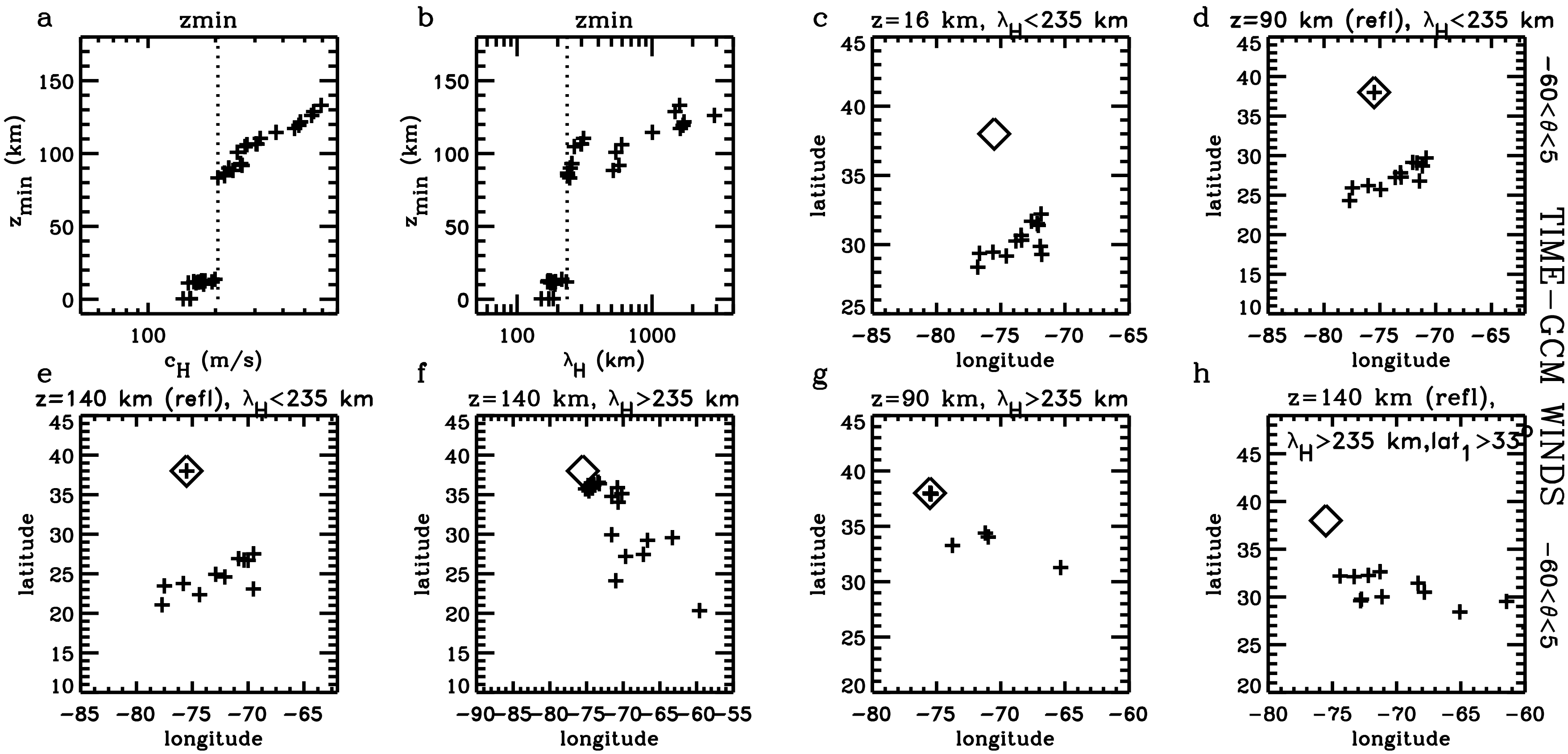

Figure 16. Reverse ray trace results using the model horizontal background winds for the 33 GWs propagating NW/Nward. (a) $z_{\min}$ as a function of c_H. The dotted line shows $c_H = 205$ m/s. (b) $z_{\min}$ as a function of λ_H. The dotted line shows $\lambda_H = 235$ km. (c) Locations of the GWs with $\lambda_H < 235$ km at $z = 16$ km. (d) Locations of the GWs from Figure 16c after continuing reverse ray tracing to $z = 90$ km. These GWs reflected at $z_{\min}$, and are therefore initially downward-propagating. (e) Locations of the GWs from Figure 16d after continuing reverse ray tracing to $z = 140$ km. (f) Locations of the initially upward-propagating GWs with $\lambda_H > 235$ km at $z = 140$ km. (g) Locations of the GWs from Figure 16f after continuing reverse ray tracing to $z = 90$ km. (h) Locations of only those GWs that are N of 33° in Figure 16f at $z = 140$ km. These GWs reflected at $z_{\min}$, and are therefore initially downward-propagating. The diamonds in Figures 16c–16h show Wallops Island.

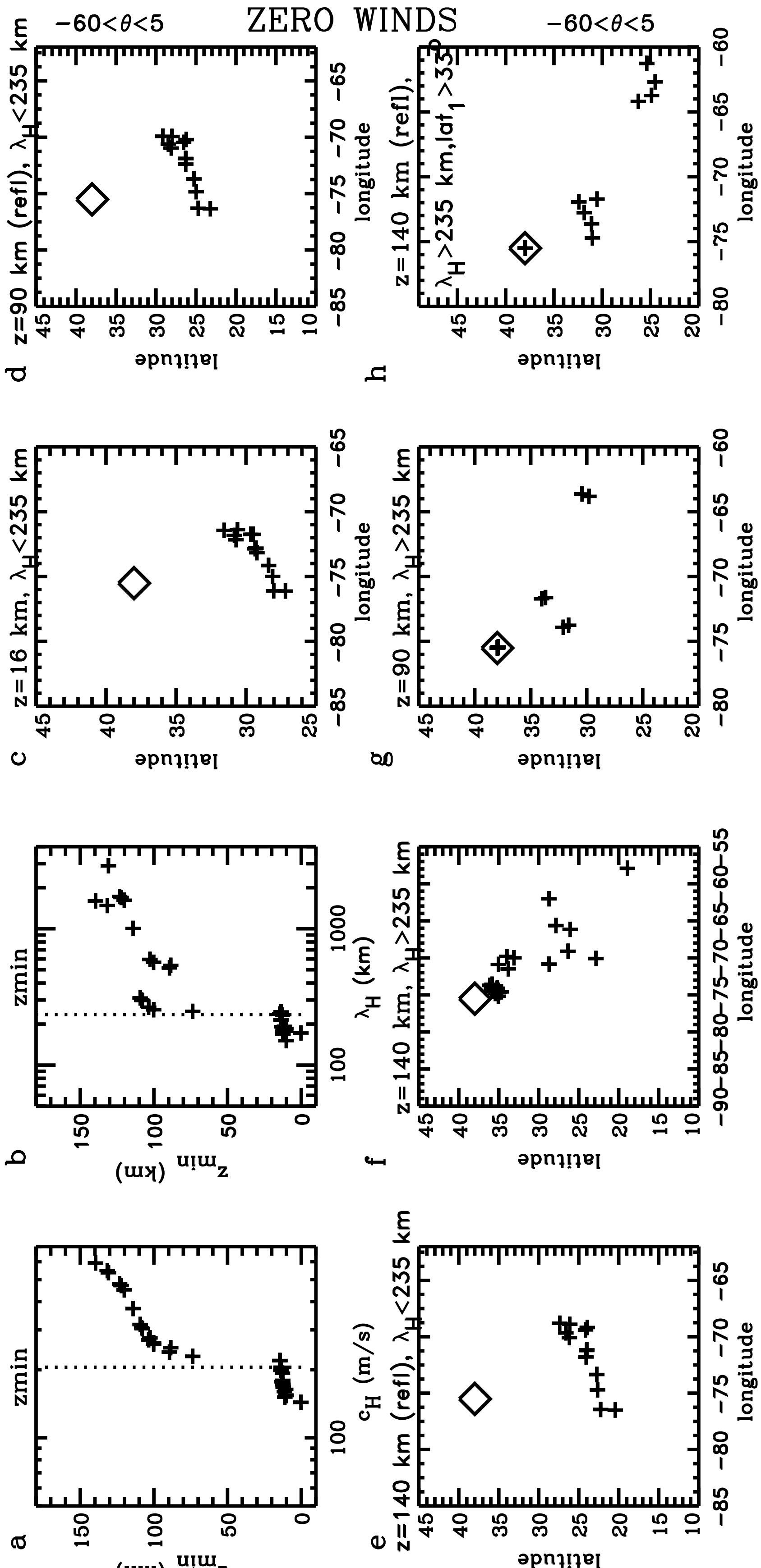

Figure 17. The same as in Figure 16, but for zero background winds, $U = V = 0$.

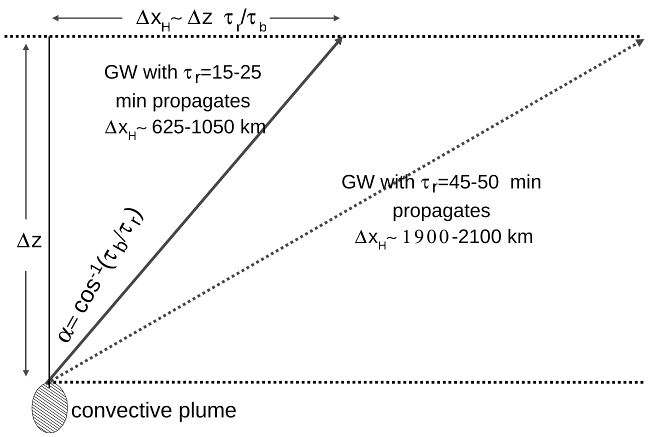

Figure 18. Sketch showing how the angle α and the horizontal distance traveled Δx_H are related to the GW period τ_r, buoyancy period τ_b, and vertical distance traveled Δz for a windless, isothermal, Boussinesq atmosphere.

reflect at $z_{\min}$ in the upper mesosphere or thermosphere, and continue reverse ray tracing backwards in time until they re-reach z = 140 km. Figure 16h shows the locations of these waves at z = 140 km if they are initially downward-propagating secondary GWs. 10 of these locations overlap well with the thermospheric body forces in Figure 11. (Note that because the "11th GW" at ~29°S and ~61°W is only slightly outside the thermospheric body force region, it might also have been excited by a thermospheric body force.) Therefore, we conclude that these 10 waves were initially downward-propagating secondary GWs from thermospheric body forces.

[50] Summarizing, Figure 16 shows that most (27) of the 33 NW/Nward propagating GWs observed by TIDDBIT were likely secondary GWs from thermospheric body forces. Three of the GWs (with $\lambda_H \sim$ 180–230 km) could have instead been secondary GWs from mesospheric body forces, although this is much less likely. Due to the large distance between Wallops Island and TS Noel, none of the GWs are identified as primary GWs excited directly by deep convective overshoot. 11 of these GWs have c_H < 205 m/s and λ_H < 235 km, and are identified as initially downward-propagating secondary GWs from thermospheric body forces. For the GWs with c_H > 205 m/s and λ_H > 235 km, 6 and 10 are identified as initially upward and downward-propagating secondary GWs from thermospheric body forces, respectively.

[51] In order to estimate how the results are affected by errors in the winds, we now show the reverse ray trace results using zero winds. Here, we retain the body force regions calculated with the model winds, because zero winds yield zero net body forces. Figure 17 shows the same results as Figure 16, but for zero winds. The sharp transition in c_H and λ_H occur at similar values as in Figure 16. Figure 17c shows similar touchdown locations as in Figure 16c, implying that none of the GWs are primary waves. The locations of the waves in Figure 17d are ~1–2°S of the same waves in Figure 16d, implying that four GWs may have arisen from mesospheric body forces. (Three are the same as for the model winds.) Figure 17e shows that the location of 13 GWs lie within the thermospheric body force source region at z = 140 km. These include the 4 GWs from Figure 17d. 11 of these 13 GWs are the same as in the model wind case. From Figure 17f, we find that the same GWs as from Figure 16f are identified as initially upward-propagating secondary GWs from thermospheric body forces. Figure 17g shows that no initially upward-propagating GWs from mesospheric body forces were observed at Wallops Island by TIDDBIT. Finally, Figure 17h shows that 8 GWs with λ_H > 235 km are identified as initially downward-propagating secondary GWs. These 8 are part of the 10 identified from Figure 16h in the model wind case. For zero winds, then, 27 GWs are identified as likely being secondary GWs from thermospheric body forces. Four could have instead been secondary GWs from mesospheric body forces, although this is less likely. Only 4 of the 27 waves are different from the model wind case. Therefore, we conclude that our results are not very sensitive to wind errors of order ~50 m/s or less.

5.4. Error in Calculating the Horizontal Distance Traveled

[52] We now estimate our error in calculating the GW locations via reverse ray tracing (since we assumed that $\nu = 0$). Dissipation affects a GW's λ_z within ~(1–2)H above and below $z_{\rm diss}$. Therefore, the total vertical propagation distance affected is $\Delta z \sim$ 3H. Since $\overline{T}$ is approximately constant at the observation altitude, a GW's ray path bends towards the horizontal as it dissipates [*Zhang and Yi*, 2002], with a corresponding decrease in λ_z of nearly ~2 (VF05). For GWs with $\lambda_z \ll 4\pi$H, the time taken to travel Δz is

$$\Delta t \sim \Delta z / c_{g,z} \simeq \Delta z \tau_{Ir} / \lambda_z, \tag{20}$$

which increases as the GW dissipates. The horizontal distance traveled during Δt is

$$\Delta x_H \simeq c_{g,H} \Delta t \sim (\lambda_z/\tau_b) \Delta z (\tau_{Ir}/\lambda_z) \sim \Delta z \tau_{Ir}/\tau_b. \tag{21}$$

(equation (21) agrees with equation (9) for zero background winds.) Although Δt increases as a GW dissipates, the horizontal group velocity decreases. These effects cancel for GWs with $\lambda_z \ll 4\pi$H, since the right hand side of equation (21) does not depend on λ_z. Therefore, the error made in assuming $\nu = 0$ for the horizontal GW locations are small for most of the GWs observed here.

5.5. Horizontal Propagation Distance for Primary GWs

[53] In section 5.3, we found that of the NW/Nward GWs which could have originated from convective overshoot (i.e., $z_{\min}$ < 20 km), all ray traced to locations ~500–1000 km N of TS Noel (Figure 16c). Since λ_H < 235 km (see Figure 16b), all of these GWs also had small periods of $\tau_r \sim$ 15–25 min (see Figure 12h). This is quite important. Using a simple picture, we now argue that these GWs could not have arisen directly from deep convection in TS Noel because their periods were too small.

[54] Figure 18 shows a sketch of primary GWs excited from a convective plume. The solid and dotted lines show the propagation paths of GWs with periods of $\tau_r \sim$ 15–25 min and $\tau_r \sim$ 45–50 min, respectively. In order to estimate the approximate horizontal distance traveled between the plume and the observation altitude ($z \sim$ 265 km), we assume Boussinesq, windless, isothermal conditions. Using

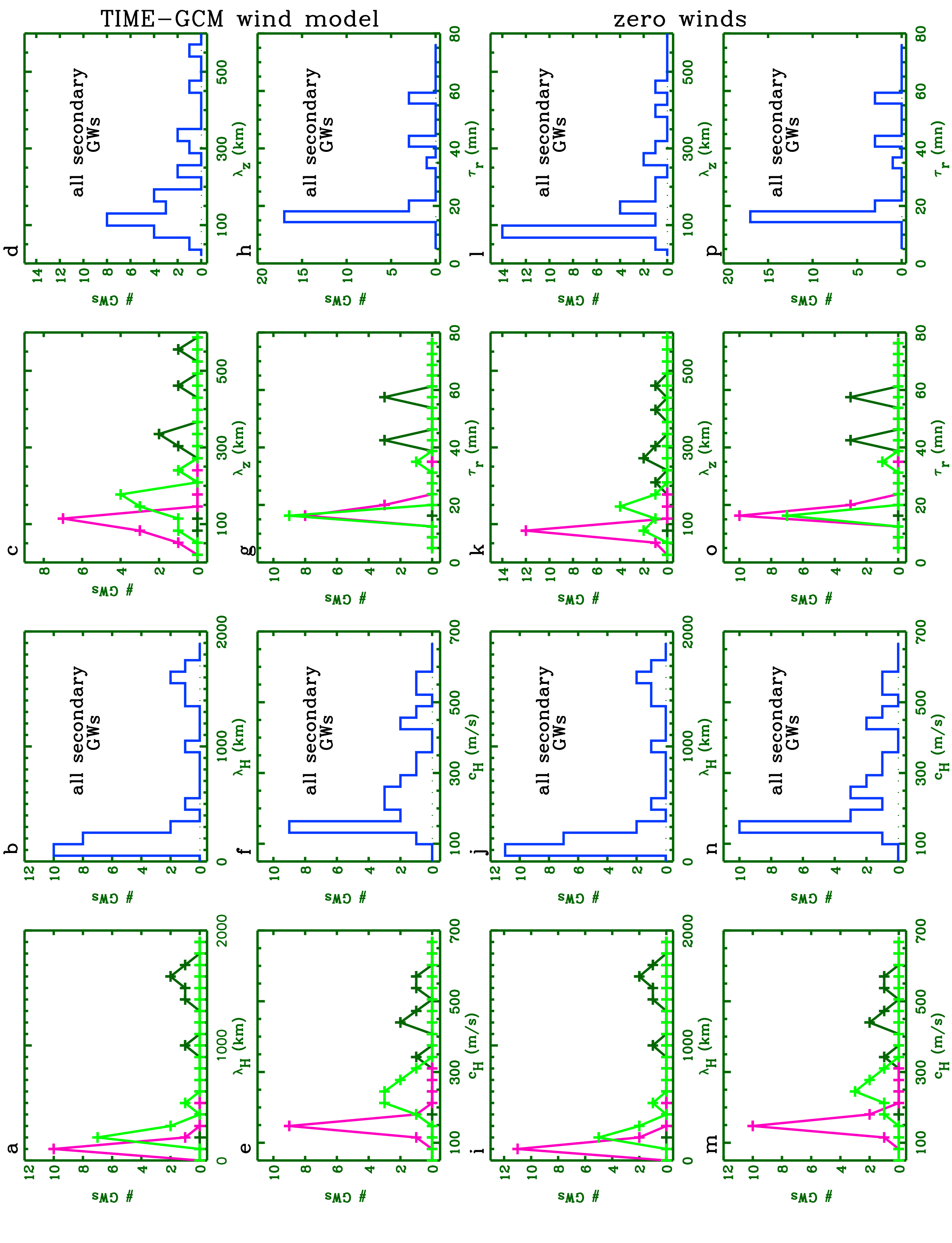
TIME−GCM wind model
zero winds
all secondary GWs
GWs
λ_H (km)
λ_z (km)
c_H (m/s)
τ_r (mn)

Figure 19

an average $\tau_b \sim 6$ min and $\Delta z \sim 250$ km, we find from equation (9) that the GW with $\tau_r \sim 15$–25 min travels horizontally $\Delta x_H \sim 625$–1050 km while propagating vertically by Δz, while the GW with $\tau_r \sim 45$–50 min travels horizontally $\Delta x_H \sim 1900$–2100 km while propagating vertically by Δz. Since none of the GWs with $z_{\min} < 20$ km had periods as large as ~45–50 min, it is not surprising that these GWs only reverse ray traced horizontally by 700–1000 km in Figure 16c, which is 500–1000 km north of TS Noel.

5.6. Largest Horizontal Propagation Distance for Secondary GWs

[55] We now estimate the largest horizontal distance that the secondary GWs observed over Wallops Island could have propagated. As is well known, those waves with the largest periods travel the largest horizontal distances (not including reflection). At the observation altitude, $N \sim 1.2 \times 10^{-2}$ rad/s from the TIME-GCM, which yields a buoyancy period of $\tau_b \sim 9$ min. Therefore, GWs with $\tau_r = 60$–90 min in a zero wind environment propagate at an angle of $90 - \alpha \sim 6$ to 9° from the horizontal plane, using equation (7). Since these secondary GWs have $\lambda_H \geq 1500$ km (see Figure 12h), they propagate to $z_{\min} \geq 110$ km before reflecting (see Figure 16b). These GWs travel from $z = 140$ km (the excitation altitude) to $z = 110$ km (the reflection altitude) to $z = 280$ km (the observation altitude), which is a total vertical distance of $\Delta z \sim 200$ km. The horizontal distance traveled during this trip is $\Delta x_H \sim \Delta z \tau_r / \tau_b \sim 2000$ km from equation (9). If a downward-propagating secondary GW has $\lambda_H < 235$ km, then it instead reflects at $z \sim 0$ to 15 km (see Figure 16b). From Figure 12h, these GWs have $\tau_r \sim 15$–25 min. Then $\Delta x_H \sim 600$–1100 km from equation (9). Therefore, for an observational limit of $\tau_r \leq 90$ min, the maximum horizontal distance that these secondary GWs (excited by thermospheric body forces at $z = 140$ km) can travel and be observed at $z \sim 280$ km is 2000 km or ~20°. This approximate horizontal limit is verified well in Figure 16, since the maximum distance from Wallops Island obtained via reverse ray tracing is ~20°.

6. Secondary GW Spectra

[56] In Figures 19a–19h, we show the wave "spectra" for the 27 NW/Nward-propagating secondary GWs excited by thermospheric body forces, as identified in section 5.3. Because these waves are ~150 km above their source altitude, Figure 19 represents the source spectrum with ~5 density scale heights of dissipative filtering. Here, we separate the secondary GWs by color, with blue showing the spectra for all 27 GWs. The pink spectra show those 11 initially downward-propagating secondary GWs which reflect near the tropopause, the light green spectra show those 10 initially downward-propagating secondary GWs which reflect in the upper mesosphere or lower thermosphere, and the dark green spectra show those 6 initially upward-propagating secondary GWs. (Note that 3 of the "pink" secondary GWs may have instead been excited by mesospheric body forces, although this is much less likely.) We see that the secondary GWs which reflect near the tropopause (pink) have smaller λ_H, c_H, and λ_z than those secondary GWs which reflect at higher altitudes (light green). Additionally, those initially upward-propagating secondary GWs (dark green) have the largest λ_H, c_H, and λ_z. In Figures 19i–19p, we show the same results as in Figures 19a–19h, but for zero winds. Although there are differences, they are reasonably small, especially for the λ_H, c_H and τ_r spectra. Therefore, we conclude that our results are reasonably robust to wind errors of order ~50 m/s or less.

[57] GW theory predicts that the characteristics of the upward and downward-propagating secondary GWs excited from horizontal body forces are the same at the source location in the intrinsic reference frame (e.g., V03). Why then are the upgoing and downgoing secondary GW spectra so different in Figure 19? The main reason is that the thermospheric body forces generated by TS Noel are located 1000–2000 km S and SE of Wallops Is. This large distance selects the characteristics of the GWs which can propagate to $z = 265$ km over Wallops Island. If a downgoing secondary GW is excited, it must propagate fairly steeply (with a relatively high frequency) down to $z_{\min}$, then back up to the observation altitude above Wallops Island. An upgoing secondary GW with the same period would propagate to the observation altitude far south of Wallops Island. Instead, only those longer period (larger λ_H) upgoing secondary GWs can propagate to the observation altitude above Wallops Island. Thus, the large distance between Wallops Island and the thermospheric body forces dictates that the observed upgoing and downgoing secondary GWs have different wave properties. This is why the "pink" GWs have smaller τ_r and c_H than the "light green" GWs, which in turn have smaller τ_r and c_H than the "dark green" GWs. Note that all of the upward-propagating GWs have $\lambda_H > 1000$ km and $\tau_r > 40$ min. Had the storm been closer, upward propagating GWs with $\lambda_H \sim$ few hundred-1000 km and $\tau_r < 40$ min would likely have been observed.

[58] In Figures 19a–19h, the combined secondary GW spectra (~150 km above the source altitude) peaks at $\lambda_H \sim 100$–300 km, $\lambda_z \sim 50$–200 km, $c_H \sim 100$–300 m/s, and $\tau_r \sim 15$–25 min. These GWs are therefore very similar to the primary GWs (excited directly by deep convection) which are known to propagate well into the thermosphere (V07; VL09). As argued in section 3.4, we expect the excited secondary GWs to peak at $\lambda_H \sim 100$–400 km and $\tau_r \sim 10$–20 min because of the spatial and temporal variability of the thermospheric body forces. Therefore, the peaks in Figures 19a–19h are consistent with the thermospheric body forces from Figure 11. Additionally, the double peak in the secondary wave spectrum for λ_H is likely an artifact of the "missing" upward propagating secondary GWs with $\lambda_H \sim$ few hundred-1000 km.

[59] Figure 20a shows the 2D secondary GW spectrum as a function of λ_H and λ_z. Although the secondary GW spectrum peaks at $\lambda_H \sim 100$–300 km and $\lambda_z \sim 50$–200 km, it has a long tail extending out to $\lambda_H \sim 2000$ km and $\lambda_z \sim$

Figure 19. Binned numbers of GWs (pluses) as a function of (a) λ_H, (c) λ_z, (e) c_H, and (g) τ_r for the GWs with $-58° \leq \theta \leq 5°$. Dark green shows the initially upward-propagating secondary GWs, pink shows the initially-downward-propagating secondary GWs with $\lambda_H < 235$ km, and light green shows the initially-downward-propagating secondary GWs with $\lambda_H > 235$ km. (b, d, f, and h) The blue lines show histograms of the total binned secondary GWs. (i–p) Same as in Figures 19a–19h, but for zero winds.

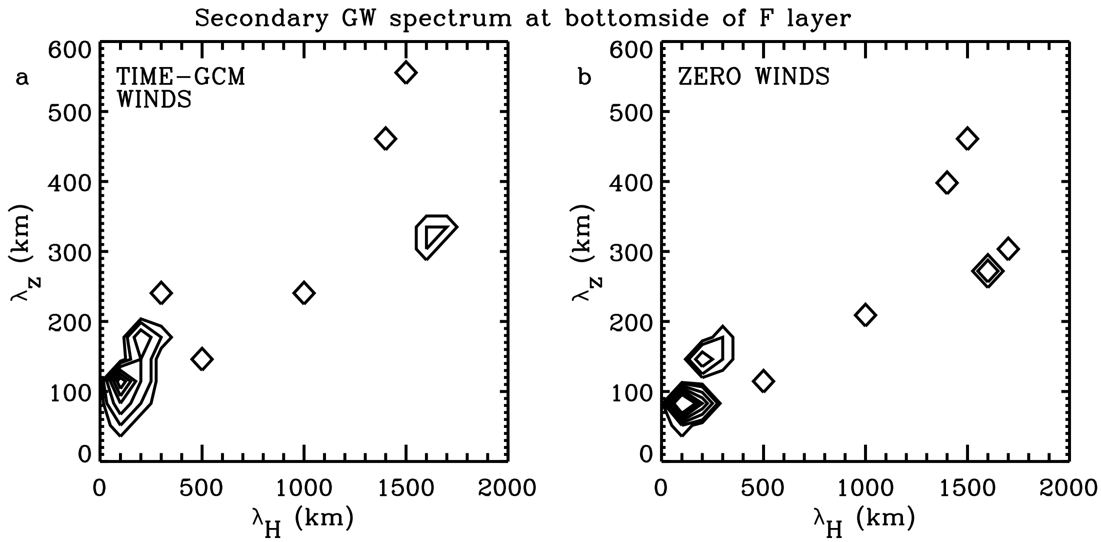

Figure 20. (a) Contour plot of the numbers of secondary GWs at the observation altitude (from Figures 19b and 19d). Contours are in units of 1. (b) Same as in Figure 20a, but for zero winds (from Figures 19j and 19l).

600 km. Because this spectrum is ~150 km above the estimated source altitude of $z \sim 140$ km, it has already undergone substantial dissipative filtering (V07), and so does not equal the secondary GW "source" spectrum. Figure 20b shows the same spectrum as Figure 20a, but for zero winds. We see that the results quite similar. Therefore, we again conclude that our results do not depend significantly on wind errors of order ~50 m/s or less.

7. Conclusions

[60] In this paper, we determined the location of the deep convective plumes and clusters which overshot the tropopause in and near TS Noel using a GOES satellite image colorized for temperature at 0432 UT on 30 October 2007. We then modeled the GWs excited by these convective objects, and ray traced the GWs into the stratosphere, mesosphere, and thermosphere. We included parameterized GW breaking. This was necessary because of the extremely large plume updraft velocities and the large numbers of clusters. We then calculated the resulting mesospheric and thermospheric body forces. We found that the mesospheric body force region was horizontally confined near TS Noel due to critical level filtering of slow waves with $c_H < 15$ m/s. In contrast, the thermospheric body force region was quite broad horizontally, was located at an average altitude of $z \sim 140$ km, extended 10° north of TS Noel, and had variability on small horizontal scales of ~100 km and small temporal scales of <15 minutes. The variability on smaller horizontal and temporal scales calculated here (as compared to VF06 or VL09, where we modeled single convective plumes) occurred because of the constructive and destructive interference of the intersecting wave fronts from differing clusters and plumes. The regions of (1) convective overshoot, (2) mesospheric body forces, and (3) thermospheric body forces determined from this ray tracing study was crucial for identifying the sources of the NW/Nward TIDDBIT waves.

[61] We then analyzed the characteristics and sources of the 59 TIDs observed at the bottomside of the F layer with $15 \le \tau_r \le 90$ min by the TIDDBIT ionospheric sounder (G. Crowley and F. Rodrigues, manuscript in preparation, 2010). We found that the majority of these TIDs were propagating NW/Nward, from the direction of TS Noel. No closer source of convective overshoot was present. Via detailed comparison with GW dissipative theory, we found that these TIDs were likely GWs. 40% of these NW/Wward propagating GWs were found to have phase speeds which were too large to have originated from convective overshoot. Therefore, we postulated that these waves must have originated in the upper mesosphere or thermosphere. A southern auroral source was ruled out for this data set, because GWs with $\tau_r \le 90$ min can only propagate to Wallops Island from a thermospheric source that is within ~20° south of Wallops Island. Alternative upper mesospheric and thermospheric sources were investigated: body forces (or accelerations) created from the breaking and/or dissipation of the small and medium-scale GWs excited by deep convection in TS Noel. These processes are known to generate intermittent mesospheric and thermospheric body forces [*Fritts and Alexander*, 2003; V03; *Vadas and Fritts*, 2004; VF06]. Because these body forces turn on and off rapidly, the fluid radiates secondary GWs in response, which propagate upwards and downwards away from the body forces (V03; VL09).

[62] Next, we reverse ray traced those GWs propagating NW/Nward (if possible) (1) directly to $z = 140$ km and $z = 90$ km from the observation altitude; (2) directly to $z_{\mathrm{trop}} + 1$ km from the observation altitude; and (3) to $z_{\min}$, then back upwards to $z = 90$ km and $z = 140$ km. Here, $z_{\min}$ was the minimum altitude that a GW could ray trace to (i.e., the altitude that an initially downward-propagating GW would reflect at). We then compared the locations determined in (1), (2) and (3) with the locations of convective overshoot in TS Noel and with the regions encompassed by the calculated mesospheric and thermospheric body forces. If a GW's location in (1) matched with the thermospheric (mesospheric) body force region, then it was identified as an initially

upward-propagating secondary GW from a thermospheric (mesospheric) horizontal body force. If a GW's location in (2) matched with convective overshoot, then it was identified as a primary GW excited directly by deep convection. Finally, if a GW's location in (3) matched with the thermospheric (mesospheric) body force region, then it was identified as an initially downward-propagating secondary GW from a thermospheric (mesospheric) body force.

[63] First, we found that only those NW/Nward TIDDBIT GWs with $c_H < 205$ m/s and $\lambda_H < 235$ km could have originated from deep convection, because they reverse ray-traced to near the tropopause; all faster/larger waves reverse ray traced no lower than the upper mesosphere prior to reflecting upwards. Second, and perhaps most importantly, we found that these GWs reverse ray traced to the tropopause 500–1000 km N of convective overshoot in TS Noel. We also found that TS Noel was the nearest source of convective overshoot S and SE of Wallops Island. Because TS Noel was 1700–2000 km S of Wallops Island at that time, we showed that a primary GW would have to have a large period of ~45–50 min to reach Wallops Island at the observation altitude. But all of the GWs which reverse ray traced to the tropopause had periods $\tau_r \leq 25$ min; we showed that these waves could only travel ~625–1050 km horizontally while propagating to the observation altitude. Therefore, we concluded that none of these relatively slower GWs were primary GWs.

[64] Second, we found that 11 of the waves with $c_H <$ 205 m/s and $\lambda_H < 235$ km reverse ray traced (after reflecting near the ground or tropopause) to $z = 140$ km at locations which overlapped with the locations of the thermospheric body forces from TS Noel. These waves were therefore identified as initially downward-propagating secondary GWs from these thermospheric body forces. Because these waves have $c_H < 250$ m/s, it is of interest to note that these waves might have been previously misidentified as originating near the tropopause [e.g. *Hocke and Schlegel*, 1996].

[65] Third, for the GWs which could not have originated from deep convection (i.e., $c_H > 205$ m/s and $\lambda_H > 235$ km), we identified 6 as initially upward-propagating secondary GWs from thermospheric body forces, and 10 as initially downward-propagating secondary GWs from thermospheric body forces. Note that because of the large distance between TS Noel and Wallops, all of the upward-propagating GWs had $\lambda_H > 1000$ km and $\tau_r > 40$ min. Had the storm been closer, upward propagating GWs with $\lambda_H \sim$ few hundred-1000 km would likely have been observed. Thus, the double peak in the secondary wave spectrum for λ_H is likely an artifact of these "missing" waves.

[66] In total, we identified 27 out of 33 NW/Nward GWs as being secondary GWs from thermospheric body forces. (3 of these may have instead been initially downward propagating secondary GWs from mesospheric body forces, although this is much less likely.) Combining these secondary GWs, we generated secondary GW spectra. We found that these spectra peak at $\lambda_H \sim 100$–300 km, $\lambda_z \sim 50$–200 km, $\tau_r \sim$ 15–25 min, and $c_H \sim 100$–300 m/s. Additionally, the spectra have long tails extending to $\lambda_H \sim 2000$ km, $c_H \sim 650$ m/s, $\tau_r \sim$ 60 min, and $\lambda_z \sim 600$ km. We have also found that this result is reasonably robust for wind errors less than ~50 m/s. Because this wave spectrum is at the bottomside of the F layer (~150 km above the source altitude), dissipative filtering has likely altered the secondary wave spectrum substantially (V07). We note here that a recent study shows reasonably good agreement between the spectrum of horizontal wavelengths of these secondary waves (Figure 19b), and the spectrum of spacings between periodic equatorial plasma bubbles (EPBs) during the summertime [*Makela et al.*, 2010]. To our knowledge, this study identifies and quantifies, for the first time, the characteristics of secondary GWs from thermospheric body forces.

[67] **Acknowledgments.** S.L.V. would like to thank Pete Stamus at CoRA/NWRA for Figures 4 and 5a, and for the convective plume/cluster parameters. S.L.V. was supported by NASA contracts NNH08CE12C and NNH07CC81C. G.C. was supported by NASA LCAS grant NG04WC22G.

[68] Robert Lysak thanks Robert Vincent and another reviewer for their assistance in evaluating this paper.

References

Alexander, M. J., J. R. Holton, and D. R. Durran (1995), The gravity wave response above deep convection in a squall line simulation, *J. Atmos. Sci.*, *52*, 2212–2226.

Andrews, D. G., J. R. Holton, and C. B. Leovy (1987), *Middle Atmosphere Dynamics*, Academic, Orlando, Florida.

Beres, J. H. (2004), Gravity wave generation by a three-dimensional thermal forcing, *J. Atmos. Sci.*, *61*, 1805–1815.

Bristow, W. A., R. A. Greenwald, and J. C. Samson (1994), Identification of high-latitude acoustic gravity wave sources using the Goose Bay HF radar, *J. Geophys. Res.*, *99*, 319–331.

Crowley, G., and I. W. McCrea (1988), A synoptic study of TIDs observed in the UK during the first WAGS campaign, October 10–18, 1985, *Radio Sci.*, *23*, 905–917.

Crowley, G., T. B. Jones, and J. R. Dudeney (1987), Comparison of short period TID morphologies in Antarctica during geomagnetically quiet and active intervals, *J. Atmos. Terr. Phys.*, *49*, 1155–1162.

Crowley, G., et al. (2006a), Global thermosphere-ionosphere response to onset of 20 November 2003 magnetic storm, *J. Geophys. Res.*, *111*, A10S18, doi:10.1029/2005JA011518.

Crowley, G., T. J. Immel, C. L. Hackert, J. Craven, and R. G. Roble (2006b), The effect of IMF by on thermospheric composition at high and middle latitudes: 1. Numerical experiments, *J. Geophys. Res.*, *111*, A10311, doi:10.1029/2005JA011371.

Djuth, F. T., M. P. Sulzer, J. H. Elder, and V. B. Wickwar (1997), High-resolution studies of atmosphere-ionosphere coupling at Arecibo Observatory, Puerto Rico, *Radio Sci.*, *32*, 2321–2344, doi:10.1029/97RS02797.

Djuth, F. T., M. P. Sulzer, S. A. Gonzales, J. D. Mathews, J. H. Elder, and R. L. Walterscheid (2004), A continuum of gravity waves in the Arecibo thermosphere?, *Geophys. Res. Lett.*, *31*, L16801, doi:10.1029/2003GL019376.

Fritts, D. C. (1982), Shear excitation of atmospheric gravity waves, *J. Atmos. Sci.*, *39*, 1936–1952.

Fritts, D. C., and M. J. Alexander (2003), Gravity wave dynamics and effects in the middle atmosphere, *Rev. Geophys.*, *41*(1), 1003, doi:10.1029/2001RG000106.

Fritts, D. C., and Z. Luo (1992), Gravity wave excitation by geostrophic adjustment of the jet stream, Part 1: Two-dimensional forcing, *J. Atmos. Sci.*, *49*, 681–697.

Fritts, D. C., and S. L. Vadas (2008), Gravity wave penetration into the thermosphere: Sensitivity to solar cycle variations and mean winds, *Ann. Geophys.*, *26*, 3841–3861.

Gossard, E. E., and W. H. Hooke (1975), *Waves in the Atmosphere*, 456 pp. Elsevier, Amsterdam, Netherlands.

Hagan, M. E., M. D. Burrage, J. M. Forbes, J. Hackney, W. J. Randel and X. Zhang (1999), GSWM-98: Results for migrating solar tides, *J. Geophys. Res.*, *104*, 6813–6827, doi:10.1029/1998JA900125.

Hines, C. O. (1967), On the nature of travelling ionospheric disturbances launched by low-altitude nuclear explosions, *J. Geophys. Res.*, *72*, 1877–1882.

Hines, C. O. (1972), Momentum deposition by atmospheric waves, and its effects on thermospheric circulation, *Space Res.*, *12*, 1157–1161.

Hocke, K., and K. Schlegel (1996), A review of atmospheric gravity waves and traveling ionospheric disturbances: 1982–1995, *Ann. Geophys.*, *14*, 917–940.

Horinouchi, T., T. Nakamura, and J. Kosaka (2002), Convectively generated mesoscale gravity waves simulated throughout the middle atmosphere, *Geophys. Res. Lett.*, *29*(21), 2007, doi:10.1029/2002GL016069.
Jones, W. (1969), Ray tracing for internal gravity waves, *J. Geophys. Res.*, *74*, 2028–2033.
Kamide, K., and A. D. Richmond (1982), Ionospheric conductivity dependence of electric fields and currents estimated from magnetic observations, *J. Geophys. Res.*, *87*, 8331–8337.
Kundu, P. (1990), *Fluid Dynamics*, 638 pp., Academic, San Diego, Calif.
Lane, T. P., M. J. Reeder, and T. L. Clark (2001), Numerical modeling of gravity waves generated by deep tropical convection, *J. Atmos. Sci.*, *58*, 1249–1274.
Lane, T. P., R. D. Sharman, T. L. Clark, and H.-M. Hsu (2003), An Investigation of turbulence generation mechanisms above deep convection, *J. Atmos. Sci.*, *60*, 1297–1321.
Larsen, M. F., and C. G. Fesen (2009), Accuracy issues of the existing thermospheric wind models: Can we rely on them in seeking solutions to wind-driven problems?, *Ann. Geophys.*, *27*, 2277–2284.
Lindzen, R. S. (1981), Turbulence and stress owing to gravity wave and tidal breakdown, *J. Geophys. Res.*, *86*, 9707–9714.
Luo, Z., and D. C. Fritts (1993), Gravity wave excitation by geostrophic adjustment of the jet stream, Part II: Three-dimensional forcing, *J. Atmos. Sci.*, *50*, 104–115.
Makela, J. J., S. L. Vadas, R. Muryanto, T. Duly, and G. Crowley (2010), Periodic spacing between consecutive equatorial plasma bubbles, *Geophys. Res. Lett.*, doi:10.1029/2010GL043968, in press.
Marks, C. J., and S. D. Eckermann (1995), A three-dimensional nonhydrostatic ray-tracing model for gravity waves: Formulation and preliminary results for the middle atmosphere, *J. Atmos. Sci.*, *52*, 1959–1984.
Oliver, W. L., Y. Otsuka, M. Sato, T. Takami, and S. Fukao (1997), A climatology of *F* region gravity wave propagation over the middle and upper atmosphere radar, *J. Geophys. Res.*, *102*, 14,499–14,512, doi:10.1029/97JA00491.
Piani, C., D. Durran, M. J. Alexander, and J. R. Holton (2000), A numerical study of three dimensional gravity waves triggered by deep tropical convection, *J. Atmos. Sci.*, *57*, 3689–3702.
Richards, P. G., J. A. Fennelly, and D. G. Torr (1994), EUVAC: A solar EUV flux model for aeronomic calculations, *J. Geophys. Res.*, *99*, 8981–8992, doi:10.1029/94JA00518.
Richmond, A. D. (1978), Gravity wave generation, propagation, and dissipation in the thermosphere, *J. Geophys. Res.*, *83*, 4131–4145.
Richmond, A. D. (1992), Assimilative mapping of ionospheric electrodynamics, *Adv. Space Res.*, *12*, 59–68.
Richmond, A. D., and Y. Kamide (1988), Mapping electrodynamic features of the high-latitude ionosphere from localized observations technique, *J. Geophys. Res.*, *93*, 5741–5759, doi:10.1029/JA093iA06p05741.
Roble, R. G., and E. C. Ridley (1994), A thermosphere-ionosphere-mesosphere-electrodynamics general circulation model (TIME-GCM): Equinox solar cycle minimum simulations (30–500 km), *Geophys. Res. Lett.*, *21*, 417–420, doi:10.1029/93GL03391.
Rottger, J. (1977), Travelling disturbances in the equatorial ionosphere and their association with penetrative cumulus convection, *J. Atmos. Terr. Phys.*, *39*, 987–998.
Salby, M. L., and R. R. Garcia (1987), Transient response to localized episodic heating in the tropics. Part 1. Excitation and short-time near-field behavior, *J. Atmos. Sci.*, *44*, 458–497.
Samson, J. C., R. A. Greenwald, J. M. Ruohoniemi, and K. B. Baker (1989), High-frequency radar observations of atmospheric gravity waves in the high-latitude ionosphere, *Geophys. Res. Lett.*, *16*, 875–878.
Samson, J. C., R. A. Greenwald, J. M. Ruohoniemi, A. Frey, and K. B. Baker (1990), Goose Bay Radar observations of Earth-reflected atmospheric gravity waves in the high-latitude ionosphere, *J. Geophys. Res.*, *95*, 7693–7709.
Smith, S. A., D. C. Fritts, and T. E. VanZandt (1987), Evidence for a saturated spectrum of atmospheric gravity waves, *J. Atmos. Sci.*, *44*, 1404–1410.
Stull, R. B. (1976), Internal gravity waves generated by penetrative convection, *J. Atmos. Sci.*, *33*, 1279–1286.
Vadas, S. L. (2007), Horizontal and vertical propagation and dissipation of gravity waves in the thermosphere from lower atmospheric and thermospheric sources, *J. Geophys. Res.*, *112*, A06305, doi:10.1029/2006JA011845.
Vadas, S. L., and D. C. Fritts (2001), Gravity wave radiation and mean responses to local body forces in the atmosphere, *J. Atmos. Sci.*, *58*, 2249–2279.
Vadas, S. L., and D. C. Fritts (2004), Thermospheric responses to gravity waves arising from mesoscale convective complexes, *J. Atmos. Sol. Terr. Phys.*, *66*, 781–804.
Vadas, S. L., and D. C. Fritts (2005), Thermospheric responses to gravity waves: Influences of increasing viscosity and thermal diffusivity, *J. Geophys. Res.*, *110*, D15103, doi:10.1029/2004JD005574.
Vadas, S. L., and D. C. Fritts (2006), Influence of solar variability on gravity wave structure and dissipation in the thermosphere from tropospheric convection, *J. Geophys. Res.*, *111*, A10S12, doi:10.1029/2005JA011510.
Vadas, S. L., and D. C. Fritts (2009), Reconstruction of the gravity wave field from convective plumes via ray tracing, *Ann. Geophys.*, *27*, 147–177.
Vadas, S. L., and H. Liu (2009), Generation of large-scale gravity waves and neutral winds in the thermosphere from the dissipation of convectively-generated gravity waves, *J. Geophys. Res.*, *114*, A10310, doi:10.1029/2009JA014108.
Vadas, S. L., and M. J. Nicolls (2009), Temporal evolution of neutral, thermospheric winds and plasma response using PFISR measurements of gravity waves, *J. Atmos. Sol. Terr. Phys.*, *71*, 740–770.
Vadas, S. L., D. C. Fritts, and M. J. Alexander (2003), Mechanism for the generation of secondary waves in wave breaking regions, *J. Atmos. Sci.*, *60*, 194–214.
Vadas, S. L., M. J. Taylor, P.-D. Pautet, P. A. Stamus, D. C. Fritts, H.-L. Liu, F. T. Sao Sabbas, V. T. Rampinelli, P. Batista, and H. Takahashi (2009a), Convection: The likely source of the medium-scale gravity waves observed in the OH airglow layer near Brasilia, Brazil, during the SpreadFEx campaign, *Ann. Geophys.*, *27*, 231–259.
Vadas, S. L., J. Yue, C.-Y. She, P. A. Stamus and A. Liu (2009b), A model study of the effects of winds on concentric rings of gravity waves from a convective plume near Fort Collins on 11 May 2004, *J. Geophys. Res.*, *114*, D06103, doi:10.1029/2008JD010753.
Waldock, J. A., and T. B. Jones (1987), Source regions of medium scale travelling ionospheric disturbances observed at mid-latitudes, *J. Atmos. Terr. Phys.*, *49*, 105–114.
Walterscheid, R. L., G. Schubert, and D. G. Brinkman (2001), Small-scale gravity waves in the upper mesosphere and lower thermosphere generated by deep tropical convection, *J. Geophys. Res.*, *106*, 31,825–31,832, doi:10.1029/2000JD000131.
Yiğit, E., A. D. Aylward, and A. S. Medvedev (2008), Parameterization of the effects of vertically propagating gravity waves for thermosphere general circulation models: Sensitivity study, *J. Geophys. Res.*, *113*, D19106, doi:10.1029/2008JD010135.
Yiğit, E., A. S. Medvedev, A. D. Aylward, P. Hartogh, and M. J. Harris (2009), Modeling the effects of gravity wave momentum deposition on the general circulation above the turbopause, *J. Geophys. Res.*, *114*, D07101, doi:10.1029/2008JD011132.
Zhang, S. D., and F. Yi (2002), A numerical study of propagation characteristics of gravity wave packets propagating in a dissipative atmosphere, *J. Geophys. Res.*, *107*(D14), 4222, doi:10.1029/2001JD000864.
Zhu, X., and J. R. Holton (1987), Mean fields induced by local gravity-wave forcing in the middle atmosphere, *J. Atmos. Sci.*, *44*, 620–630.

G. Crowley, Atmospheric and Space Technology Research Associates, 12703 Spectrum Dr., Suite 101, San Antonio, TX 78249, USA.
S. L. Vadas, Colorado Research Associates Division, NorthWest Research Associates, 3380 Mitchell Lane, Boulder, CO 80301, USA. (vasha@cora.nwra.com)